An Improved Perturbation Pressure Closure for Eddy-Diffusivity Mass-Flux Schemes

Jia He[1], Yair Cohen[1], Ignacio Lopez-Gomez[1], Anna Jaruga[1], Tapio Schneider[1,2]

[1]California Institute of Technology, Pasadena, California, USA.
[2]Jet Propulsion Laboratory, California Institute of Technology, Pasadena, California, USA.

Key Points:

- An analytical closure for the perturbation pressure in convection parameterizations is derived.
- The closure combines the effects of virtual mass, momentum advection damping, and pressure drag.
- The closure performs well in simulating a rising bubble and the diurnal cycle of deep convection.

Corresponding author: Jia He, `jiahe@caltech.edu`

Abstract

Convection parameterizations such as eddy-diffusivity mass-flux (EDMF) schemes require a consistent closure formulation for the perturbation pressure, which arises in the equations for vertical momentum and turbulence kinetic energy (TKE). Here we derive an expression for the perturbation pressure from approximate analytical solutions for 2D and 3D thermal bubbles. The new closure combines modified pressure drag and virtual mass effects with a new momentum advection damping term. This advection damping is an important source in the lower half of the thermal bubble and at cloud base levels in convective systems. It represents the effect of the perturbation pressure to ensure the non-divergent properties of the flow. The new formulation represents the pressure drag to be inversely proportional to updraft depth. This is found to significantly improve simulations of the diurnal cycle of deep convection, without compromising simulations of shallow convection. It is thus a key step toward a unified scheme for a range of convective motions. By assuming that the pressure only redistributes TKE between updrafts and the environment laterally, a closure for the velocity pressure-gradient correlation is obtained from the perturbation pressure closure. This novel pressure closure is implemented in an extended EDMF scheme and is shown to successfully simulate a rising bubble as well as shallow and deep convection in a single column model.

Plain Language Summary

Global climate models rely on subgrid-scale (SGS) parameterizations to represent heat and moisture transport by unresolved turbulent and convective motions. In this and two companion papers, the extended eddy-diffusivity mass-flux (EDMF) scheme is developed as a single unified scheme that represents all SGS turbulent and convective processes. This paper focuses on the closure for the perturbation pressure that ensures the non-divergence of the mass flux. An analytical formulation for the pressure closure is derived by considering the dynamics of a buoyant bubble. The closure differs from commonly used formulations in two respects. First, it introduces an additional momentum advection damping term that contributes a momentum source at the bubble bottom and cloud base. Second, it improves the drag term and enables the EDMF scheme to correctly reproduce the diurnal cycle of deep convection. Comparison with large-eddy simulations of moist convection and rising bubbles demonstrates the adequacy of the closure.

1 Introduction

Turbulent and convective motions play essential roles in the transport of energy and moisture in the climate system. Due to computational constraints, climate models use resolutions that are too coarse to resolve these motions and rely heavily on various parameterizations to represent their subgrid-scale (SGS) contribution to the resolved flow. Such parameterizations are one of the primary sources of model uncertainty in long-term climate projections (Bony & Dufresne, 2005; Bony et al., 2015; Brient & Schneider, 2016; Caldwell et al., 2018; Ceppi et al., 2017; Murphy et al., 2004; Teixeira et al., 2011; Webb et al., 2013). Since advances in computational resources will not suffice to fully resolve turbulent and convective motions in the foreseeable future (Schneider et al., 2017), continuous efforts to reduce the biases and uncertainties from SGS parameterizations in climate models are required.

Conventionally, SGS processes such as boundary layer turbulence, shallow convection, and deep convection have been represented by separate parameterization schemes. This leads to a discontinuous representation of processes that lie on a physical continuum. It also results in a proliferation of correlated parameters (e.g., separate entrainment rates for shallow and deep convection), which complicates the calibration of climate models. Considerable efforts have been made to develop a unified parameterization that synthesizes the SGS turbulence and convection processes into one single scheme, without artificial switches between different regimes (Lappen & Randall, 2001a, 2001c, 2001b; Larson & Golaz, 2005; Golaz et al., 2002b, 2002a; Soares et al., 2004; Siebesma et al., 2007; Park, 2014a, 2014b; Tan et al., 2018; Thuburn et al., 2018, 2019; Weller & McIntyre, 2019; Cohen et al., 2020; Lopez-Gomez et al., 2020). A challenge in the development of such a unified scheme is closing the representation of various physical processes that emerge in the development of the scheme. In the case of mass-flux parameterizations, one of the key terms requiring closure is the perturbation pressure gradient, which is the focus of this work.

Perturbation pressure, defined as the departure of pressure from a reference profile in hydrostatic balance with a reference density, plays an important role in the development of convective systems (Holton, 1973; Schumann & Moeng, 1991; Jeevanjee & Romps, 2015, 2016; Morrison, 2016b; Peters, 2016). It is an essential source/sink term for vertical momentum (Holton, 1973) and contributes to the redistribution of turbulence kinetic energy (TKE) (Heinze et al., 2015). It is typically diagnosed from a 3D Poisson equation in large-eddy simulations (LES). Its closure remains challenging for parameterization schemes (Holland & Rasmusson, 1973; Morrison, 2016b; Peters, 2016; Tarshish et al., 2018).

Theoretical studies (e.g., Holton (1973); Lappen and Randall (2006); Morrison (2016b, 2016a); Leger et al. (2019)) explicitly solve for the perturbation pressure from a set of differential equations considering both horizontal and vertical motions; they have demonstrated success in idealized simulations. Most parameterization schemes, however, do not explicitly solve for the pressure gradient term from differential equations. Instead, the perturbation pressure gradient is formulated semi-empirically as a combination of various physical processes: a virtual mass effect that effectively reduces buoyancy, a momentum sink proportional to entrainment, and a drag term inversely proportional to the horizontal scale of the updraft (Simpson & Wiggert, 1969; Siebesma et al., 2007; de Roode et al., 2012; Tan et al., 2018; Han & Bretherton, 2019; Suselj et al., 2019).

The formulation of de Roode et al. (2012) represents a pure sink for the vertical momentum of convective systems. However, in an LES study, Jeevanjee and Romps (2015) decomposed the perturbation pressure into a buoyancy perturbation pressure and a dynamic perturbation pressure. They showed that the dynamic pressure is a significant momentum source at low levels of convective systems. Peters (2016) observed a similar positive momentum forcing from the dynamic perturbation pressure in a deep convective system. While the pressure gradient structure can become more complex when the updraft consists of multiple distinct thermals (Moser & Lasher-Trapp, 2017; Morrison et al., 2020), these observed results are in contradiction to the typical pressure closures that serve merely as momentum sinks. In this paper, we demonstrate that a vertical momentum source owing to the perturbation pressure gradient is important for capturing the dynamics of an idealized rising dry bubble.

We derive a novel closure for the perturbation pressure in the extended eddy-diffusivity mass-flux (EDMF) framework (Tan et al., 2018; Cohen et al., 2020). The closure explicitly recognizes the roles of the perturbation pressure as a vertical momentum source and sink and in TKE redistribution. The extended EDMF framework and its entrainment and detrainment closures are presented in Cohen et al. (2020), and the eddy diffusivity and mixing length closures are discussed in Lopez-Gomez et al. (2020). Together with the perturbation pressure closure, these closures make the extended EDMF a unified framework that successfully simulates a wide range of turbulent and convective regimes, from stable boundary layers to deep convection, without altering any of the equation components or parameter values. Moreover, we show here that the extended EDMF scheme is also able to simulate individual convective 2D bubbles, albeit with changes in parameters and some additions to the formulation of the entrainment and detrainment closures.

The need for these changes is discussed in the context of the general difference between convective updrafts and convective bubbles.

Section 2 lays out the analytical derivation for the perturbation pressure in a 2D thermal bubble, with the 3D axisymmetric counterpart given in Appendix B. Section 3 briefly reviews the extended EDMF framework and implements the perturbation pressure closure in it. Section 4 describes the setups of a dry bubble experiment and moist convective test cases in LES and a single column model (SCM). Simulation results are shown in Section 5, their implications and limitations are discussed in Section 6. Finally, Section 7 summarizes the conclusions.

2 Vertical Perturbation Pressure Gradient

In order to decouple the derivation of the perturbation pressure structure from density changes, we use the Boussinesq approximation. (Caveats to this approach are discussed in Section 2.1.) The momentum equation in the Boussinesq approximation is written as

$$\frac{\partial \mathbf{v}}{\partial t} + \mathbf{v} \cdot \nabla \mathbf{v} = b\hat{\mathbf{k}} - \nabla \left(\frac{p^\dagger}{\rho_h} \right) + S_{\mathbf{v}}, \tag{1}$$

where t is time, $\mathbf{v} = (u, v, w)$ is the 3D velocity vector, $\hat{\mathbf{k}}$ is the vertical unit vector, ρ_h is a constant reference density, and $S_{\mathbf{v}}$ represents 3D momentum sources other than buoyancy and the pressure gradient force. The buoyancy is defined as

$$b = -g \frac{\rho - \rho_h}{\rho_h},$$

where g is the gravitational acceleration. The perturbation pressure is defined as

$$p^\dagger = p - p_h,$$

where $p_h(z)$ is the reference pressure profile in hydrostatic balance with the reference density ρ_h, i.e., $\hat{\mathbf{k}} \cdot \nabla p_h = -\rho_h g$. Note that ρ_h is a constant reference density, while p_h is height dependent.

2.1 Pressure Poisson Equation

The Boussinesq approximation implies that the velocity $\mathbf{v}$ is nondivergent. Therefore, taking the divergence of the momentum equation (1) and ignoring the source term $S_{\mathbf{v}}$ leads to a Poisson equation for the perturbation pressure

$$\nabla^2 \left(\frac{p^\dagger}{\rho_h} \right) = \frac{\partial b}{\partial z} - \nabla \cdot (\mathbf{v} \cdot \nabla \mathbf{v}). \tag{2}$$

To simplify notation, we define a pressure potential as

$$P = \frac{p}{\rho_h}. \tag{3}$$

In the remainder of this paper, we use the pressure potential P, which we generally refer to as “pressure” as it plays a similar role in the vertical momentum equation. We derive a closure for the gradient of the perturbation pressure potential, $\nabla P^\dagger$, with the dagger again denoting perturbations relative to the reference pressure potential.

It is common to decompose the perturbation pressure into the buoyancy perturbation pressure (P_b) and the dynamic perturbation pressure (P_d) (i.e., $P^\dagger = P_\mathrm{b} + P_\mathrm{d}$), associated with the two terms on the right-hand side of (2),

$$\nabla^2 P_{\mathrm{b}} = \frac{\partial b}{\partial z}, \tag{4a}$$

$$\nabla^2 P_{\mathrm{d}} = -\left[\left(\frac{\partial u}{\partial x}\right)^2 + \left(\frac{\partial v}{\partial y}\right)^2 + \left(\frac{\partial w}{\partial z}\right)^2\right] - 2\left[\frac{\partial u}{\partial y}\frac{\partial v}{\partial x} + \frac{\partial v}{\partial z}\frac{\partial w}{\partial y} + \frac{\partial w}{\partial x}\frac{\partial u}{\partial z}\right]. \tag{4b}$$

In the derivations that follow, we consider for simplicity a 2D Cartesian geometry. An analogous derivation for an axisymmetric thermal bubble in cylindrical coordinates is given in Appendix B. In the 2D geometry, with $\mathbf{v} = (u, w)$ and $\nabla^2_{x,z} = \partial^2/\partial x^2 + \partial^2/\partial z^2$, the Poisson equations (4), after using the continuity equation, become

$$\nabla^2_{x,z} P_{\mathrm{b}} = \frac{\partial b}{\partial z}, \tag{5a}$$

$$\nabla^2_{x,z} P_{\mathrm{d}} = -2\left[\left(\frac{\partial w}{\partial z}\right)^2 + \frac{\partial u}{\partial z}\frac{\partial w}{\partial x}\right]. \tag{5b}$$

Considerable efforts have been made to understand the buoyancy perturbation pressure and its impact on the effective buoyancy (Jeevanjee & Romps, 2015; Peters, 2016; Tarshish et al., 2018). For example, Tarshish et al. (2018) draw analogies between the effective buoyancy and buoyancy perturbation pressure of the fluid and the magnetic charge and potential in magnetostatics. They obtain an analytical solution for the buoyancy perturbation pressure from a homogeneous thermal with added randomness. However, they do not account for the dynamic perturbation pressure induced by the velocity field.

Here we solve the pressure Poisson equation accounting for both the buoyancy and the dynamic perturbation pressure. We consider a thermal bubble and make a single-normal mode assumption. Although the single-normal mode assumption is made for simplicity, it has proven to be successful in simulating convective systems. For example, Holton (1973) adopted a single-normal mode for the horizontal direction when solving for the perturbation pressure from a diagnostic Poisson equation. Morrison (2016b) derived a single-normal mode solution for the buoyancy perturbation pressure, making the assumption that the dynamic perturbation pressure is negligible when determining the vertical velocity within an updraft. They also derived a general solution for perturbation pressure from the steady-state momentum and mass continuity equations in presence of a lower boundary. The derivation in Morrison (2016b) shows a dependency of the pressure forcing term on the dimensionality of the convection: the pressure forcing is stronger in a 2D Cartesian setup than that in the 3D axisymmetric setup. Here we use the single-normal mode solution within an ensemble of multiple thermals.

The Boussinesq approximation is a limitation to study deep convection. Morrison (2016a) showed that although the net perturbation pressure between the cloud top and bottom differs in the Boussinesq and anelastic approximations, the vertical acceleration is much less sensitive to the approximations. This is due to compensation from the different density profiles used in the two approximations. This provides one justification for our use of the simplifying Boussinesq approximation.

2.2 Single-Normal Mode Solution

In this subsection, we derive a single-normal mode solution for the perturbation pressure for a 2D thermal in Cartesian coordinates. We assume the 2D thermal is positively buoyant and has horizontal extent $2R$ and vertical extent H. That is, its horizontal and vertical wavenumbers are $k_b = \pi/(2R)$ and $m = \pi/H$, respectively. The single-normal mode structure for buoyancy is

$$b = b_A \sin(mz)\cos(k_b x), \quad x \in [-R, R], \quad z \in [0, H], \tag{6}$$

where b_A is the normal mode amplitude for buoyancy.

We make a similar single-normal mode ansatz for the flow inside the thermal, assuming free-slip boundary conditions, that is, the vertical velocity w vanishes at the top and bottom of the thermal and the horizontal velocity u vanishes at its lateral boundaries. This configuration defines a closed circulation with an upward branch at the center of the thermal and two outlying descending branches. The velocity field has the same vertical wavenumber as the buoyancy, while its horizontal wavenumber k_w is different from k_b. The single-normal mode structure for vertical velocity is

$$w = w_A \sin(mz) \cos(k_w x), \tag{7}$$

where w_A is the normal mode amplitude for w. From the continuity equation, $\partial_x u + \partial_z w = 0$, we have

$$\frac{\partial u}{\partial x} = -\frac{\partial w}{\partial z} = -m w_A \cos(mz) \cos(k_w x), \tag{8}$$

and we set

$$u = u_A \cos(mz) \sin(k_w x), \tag{9}$$

where u_A is the normal mode amplitude for u. The free-slip boundary condition requires $k_w = 2k_b = \pi/R$; Eqs. (8) and (9) then imply

$$k_w u_A = -m w_A. \tag{10}$$

Equations (6), (7), and (9) together describe the single-normal mode structure of the buoyancy and velocity fields for the 2D thermal in Cartesian coordinates. The flow pattern that arises is shown in Figure 1. The buoyancy structure and flow fields for a 3D axisymmetric thermal in cylindrical coordinates using the Fourier-Bessel decomposition (Holton, 1973) are described in Appendix B.

2.2.1 Buoyancy Perturbation Pressure

With the normal-mode ansatz (6), the P_b Poisson equation (5a) reduces to

$$\nabla^2_{x,z} P_\mathrm{b} = \frac{\partial b}{\partial z} = m b_A \cos(mz) \cos(k_b x). \tag{11}$$

The buoyancy perturbation pressure P_b then needs to have the same trigonometric structure as the right-hand side of (11), i.e.,

$$P_\mathrm{b} = P_0 \cos(mz) \cos(k_b x). \tag{12}$$

The coefficient P_0 is obtained by substituting this form for P_b into (11), leading to

$$\nabla^2_{x,z} P_\mathrm{b} = -P_0 \left(m^2 + k_b^2\right) \cos(mz) \cos(k_b x) = m b_A \cos(mz) \cos(k_b x).$$

This gives

$$P_0 = -\frac{m}{m^2 + k_b^2} b_A.$$

Therefore, the single-normal mode solution for the buoyancy perturbation pressure is

$$P_\mathrm{b} = -\frac{m}{m^2 + k_b^2} b_A \cos(mz) \cos(k_b x), \tag{13}$$

and the buoyancy perturbation pressure gradient needed in the vertical momentum equation is

$$-\frac{\partial P_\mathrm{b}}{\partial z} = -\frac{m^2}{m^2 + k_b^2} b_A \sin(mz) \cos(k_b x) = -\frac{b}{[1 + (H/2R)^2]}. \tag{14}$$

As the bubble gets wider and shallower, a stronger virtual mass effect leads to a weaker effective buoyancy, consistent with the solution for an idealized spherical bubble with homogeneous buoyancy distribution (Tarshish et al., 2018).

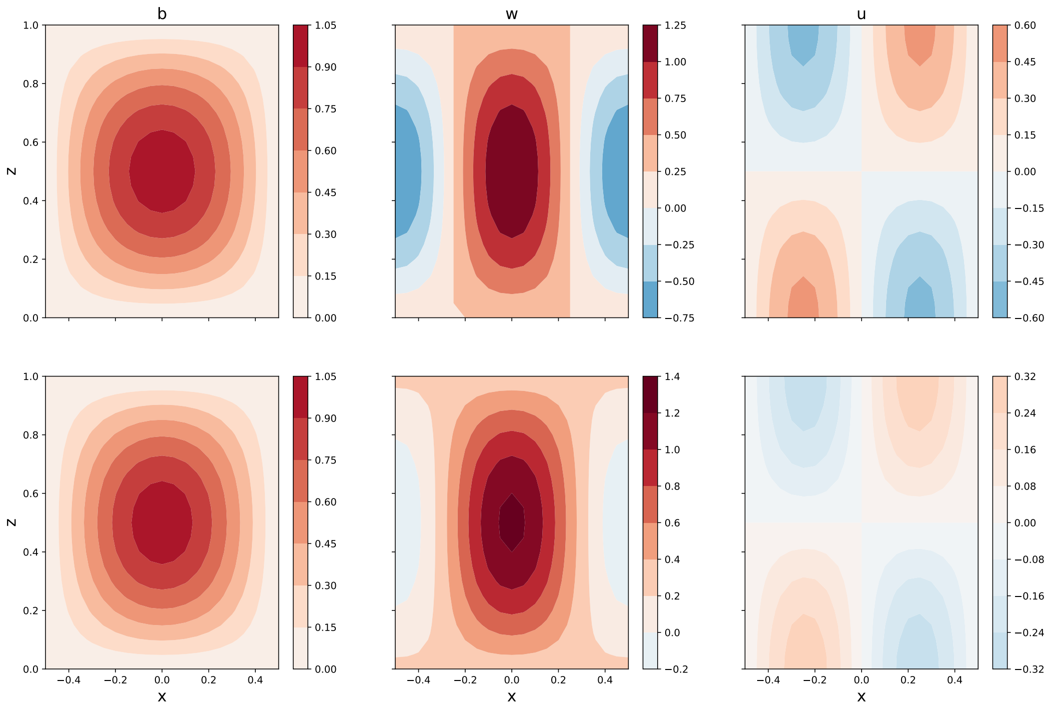

Figure 1. Buoyancy and velocity patterns for the single-normal mode ansatz for the 2D (top) and 3D (bottom) thermals. The thermal is created by specifying dimensionless parameters $2R = H = 1$ and $b_A = w_A = 1$. The velocity amplitude u_A is computed from the non-divergence criterion $k_w u_A + m w_A = 0$. The vertical velocities w in the middle column is shown the velocity from the single-normal model ansatz plus the velocity of the thermal, which is taken as 25% of the peak w at the thermal center.

2.2.2 Dynamic Perturbation Pressure

Similarly, using the ansatz (7) and (9), the Poisson equation for the dynamical pressure becomes

$$\nabla^2_{x,z} P_{\mathrm{d}} = -2\left[\left(\frac{\partial w}{\partial z}\right)^2 + \frac{\partial u}{\partial z}\frac{\partial w}{\partial x}\right] = -m^2 w_A^2 \cos(2mz) - m^2 w_A^2 \cos(2k_w x). \tag{15}$$

We assume the dynamic perturbation pressure has the form

$$P_{\mathrm{d}} = P_1 \cos(2mz) + P_2 \cos(2k_w x) + Fz + G(x, xz), \tag{16}$$

which satisfies (15). The function $G(x, xz)$ can be written in the general form $G_1 x + G_2 xz + G_3$. Since the flow is symmetric with respect to $x = 0$, the dynamic perturbation pressure induced by the flow should also be symmetric, i.e., $P_{\mathrm{d}}(x) = P_{\mathrm{d}}(-x)$. As a result, $G_1 = G_2 = 0$, and $G(x, xz) = G_3$ is a constant. Then the Laplacian of P_d is

$$\nabla^2_{x,z} P_{\mathrm{d}} = -4m^2 P_1 \cos(2mz) - 4k_w^2 P_2 \cos(2k_w x),$$

which gives $P_1 = w_A^2/4$ and $P_2 = m^2 w_A^2/(4k_w^2)$. Therefore, the dynamic perturbation pressure is

$$P_{\mathrm{d}} = \underbrace{\frac{w_A^2}{4}\cos(2mz)}_{A} + \underbrace{\frac{m^2 w_A^2}{4k_w^2}\cos(2k_w x)}_{B} + \underbrace{Fz}_{C} + \underbrace{G_3}_{D}. \tag{17}$$

The ultimate goal is to parameterize the pressure gradient force $-\partial_z P_{\mathrm{d}}$, in which the z-independent terms, B and D, do not participate. Term C in (17) may be used to describe the aerodynamic drag, alleviating the shortcomings of our simplified inviscid approximation. The form drag experienced by the thermal equals the total pressure (air pressure plus $0.5\rho|w|^2$) loss of the surrounding flow across the thermal (Liu et al., 2015), that is,

$$\int_{-R}^{R} \rho \left[P_{\mathrm{d}} + \frac{w^2}{2}\right]_{z=0}^{z=H} dx = \frac{1}{2}\rho A c_d w_r^2, \tag{18}$$

where c_d is the drag coefficient, A is the cross-sectional area perpendicular to w_r (i.e., $A = 2R$ in the 2D setup), and w_r is the velocity of the thermal relative to the environment. Using P_{d} from (17) in (18), we obtain

$$F = \frac{1}{2} c_d \frac{w_r^2}{H}, \tag{19}$$

describing the pressure drag the thermal experiences in the fluid. This drag, derived by integrating the total pressure along the boundaries of the thermal, is a result of the particular assumptions we made for the flow pattern and boundary conditions. Finally, the vertical pressure gradient force is given by

$$\begin{aligned} -\frac{\partial P_{\mathrm{d}}}{\partial z} &= \frac{m}{2} w_A^2 \sin(2mz) - \frac{1}{2} c_d \frac{w_r^2}{H} \\ &= m w_A^2 \sin(mz)\cos(mz) - \frac{1}{2} c_d \frac{w_r^2}{H} \\ &= w_A \sin(mz) \frac{d}{dz}\left[w_A \sin(mz)\right] - \frac{1}{2} c_d \frac{w_r^2}{H} \\ &= w_c \frac{dw_c}{dz} - \frac{1}{2} c_d \frac{w_r^2}{H}, \end{aligned} \tag{20}$$

where $w_c = w_A \sin(mz)$ represents the velocity at the thermal axis.

The single-normal mode assumption is a major simplification for the thermal structure and has some limitations. It approximates the thermal as a flow perturbation with positive buoyancy and trigonometric structure in both horizontal and vertical directions. Its implied internal flow has two symmetric circulation lobes, with ascending branch in the center and descending branches on the sides. This flow pattern resembles the internal flow within Hill's vortex (e.g., Levine (1959)), except that it is defined over a rectangle instead of a circle.

Figure 1 sketches out the buoyancy and velocity fields under this ansatz. Note that convection consists of a large ensemble of thermals (e.g., Sherwood et al. (2013), Romps and Charn (2015), Morrison et al. (2020)), and parameterization schemes aim at representing the statistical behavior of the ensemble. In Appendix C, we lay out a derivation for the ensemble composite of multiple thermals centered at their centroids. The analytical structure for the multi-thermal ensembles, shown in Figure C1, is consistent with the idealized simulation results in Morrison (2016b) and resembles the composite results of bubbles identified in the convective test cases (Figure 5).

Asymmetries arising from the lower boundaries and from the environment wind shear can be important in the development and maintenance of convective systems (Jeevanjee & Romps, 2016; Morrison, 2016b); they are neglected in this idealized symmetric thermal setup.

Despite these simplifications, the solutions for the buoyancy perturbation pressure P_{b} in (13) and the dynamic perturbation pressure P_{d} in (17) are consistent with idealized numerical simulations (Morrison, 2016b; Morrison & Peters, 2018).

3 Perturbation Pressure Gradient in the Extended EDMF Scheme

In the EDMF framework, a GCM grid box is divided into subdomains that consist of coherent updrafts/downdrafts and an isotropic environment. Following Cohen et al. (2020), the conditional average of a property ϕ in the i-th subdomain is denoted by $\bar{\phi}_i$, with a_i as the area fraction occupied by the subdomain. The fluctuation around the subdomain average is denoted by $\phi'_i = \phi - \bar{\phi}_i$. We use $i = 0$ for the turbulent isotropic environment and $i \geq 1$ for coherent updrafts and downdrafts. Angle brackets $\langle \phi \rangle$ denote the grid-mean average of ϕ, and $\phi^* = \phi - \langle \phi \rangle$ denotes the fluctuation around the grid mean. It is also convenient to define the difference between the subdomain average and the grid box average as $\overline{\phi}_i^* = \bar{\phi}_i - \langle \phi \rangle$. Finally, the grid box average is related to the subdomain average by the area-weighted average over all subdomains:

$$\langle \phi \rangle = \sum_i a_i \bar{\phi}_i. \tag{21}$$

Using Reynolds averaging rules and this subdomain decomposition, SGS vertical fluxes are decomposed into the sum of subdomain-average components and components owing to fluctuations within the subdomains:

$$\langle w^* \phi^* \rangle = \sum_i a_i (\overline{w}_i^* \overline{\phi}_i^* + \overline{w'_i \phi'_i}). \tag{22}$$

The first term is represented by mass flux closures while the second term is taken to be nonzero only for the turbulent environment ($i = 0$); it is modeled as downgradient eddy diffusion, hence name of the eddy-diffusivity mass-flux (EDMF) scheme. Accurate parameterization of this SGS vertical flux is the key goal of the EDMF scheme.

The full set of equations solved by the extended EDMF scheme is discussed in Cohen et al. (2020). For the purpose of understanding the role of perturbation pressure, here we briefly lay out the vertical momentum equation for updrafts/downdrafts, and the TKE equation for the environment, in which the perturbation pressure arises.

3.1 Updraft Vertical Velocity and Environmental TKE in the Extended EDMF Scheme

The vertical momentum equation for the i-th subdomain is

$$\begin{aligned}\frac{\partial(\rho a_i \bar{w}_i)}{\partial t} + \nabla_h \cdot (\rho a_i \langle \mathbf{u}_h \rangle \bar{w}_i) + \frac{\partial(\rho a_i \bar{w}_i \bar{w}_i)}{\partial z} = &\underbrace{\frac{\partial}{\partial z}\left(\rho a_i K_{w,i} \frac{\partial \bar{w}_i}{\partial z}\right)}_{\text{turbulent flux}} \\ &+ \underbrace{\sum_{j \neq i}\left[\left(E_{ij} + \hat{E}_{ij}\right)\bar{w}_j - \left(\Delta_{ij} + \hat{E}_{ij}\right)\bar{w}_i\right]}_{\text{entrainment/detrainment}} + \underbrace{\rho a_i \bar{b}_i^* + \rho a_i \langle b \rangle}_{\text{buoyancy}} \\ &\underbrace{-\rho a_i \overline{\left(\frac{\partial P^\dagger}{\partial z}\right)}_i^* - \rho a_i \frac{\partial \langle P^\dagger \rangle}{\partial z}}_{\text{perturbation pressure}},\end{aligned} \tag{23}$$

where $\mathbf{u}_h$ is the horizontal component of the velocity vector, whose subdomain value is taken to be equal to its grid-mean value. Following Cohen et al. (2020), $\rho = \langle \rho \rangle$ is the grid-mean density. The exchange of mass is represented by dynamical entrainment, E_{ij}, dynamical detrainment, Δ_{ij}, and turbulent entrainment, $\hat{E}_{ij}$; see Cohen et al. (2020) for details. Vertical turbulent fluxes are represented by the eddy diffusivity $K_{w,i}$ (Lopez-Gomez et al., 2020).

The subdomain buoyancy is defined as

$$\bar{b}_i = -g \frac{\bar{\rho}_i - \rho_h}{\rho}.$$

It is decomposed into a contribution from the grid-mean buoyancy

$$\langle b \rangle = -g \frac{\rho - \rho_h}{\rho},$$

and a departure from the grid mean

$$\bar{b}_i^* = -g \frac{\bar{\rho}_i^* - \rho_h}{\rho}.$$

Similarly, the perturbation pressure gradient is decomposed into a grid-mean component and a departure from the grid mean, i.e.,

$$-\overline{\left(\frac{\partial P^\dagger}{\partial z}\right)}_i = -\frac{\partial \left\langle P^\dagger \right\rangle}{\partial z} - \overline{\left(\frac{\partial P^\dagger}{\partial z}\right)}_i^*. \tag{24}$$

In the GCM setting, the grid-mean buoyancy $\langle b \rangle$ and perturbation pressure gradient $-\partial \langle P^\dagger \rangle / \partial z$ are provided by the dynamical core; in the SCM setting, they are balanced as in Eq. (47) in Cohen et al. (2020). The subdomain buoyancy relative to the grid mean, $\bar{b}_i^*$, is computed from the density using a nonlinear saturation adjustment; see the appendix in Pressel et al. (2015). Here we develop a closure scheme for the subdomain perturbation pressure, $-\overline{(\partial P^\dagger / \partial z)}_i^*$.

The subdomain TKE is defined as $\bar{e}_i = 0.5(\overline{u_i'^2}+\overline{v_i'^2}+\overline{w_i'^2})$, and the environmental ($i=0$) TKE equation is

$$\frac{\partial(\rho a_0 \bar{e}_0)}{\partial t} + \nabla_h \cdot (\rho a_0 \langle \mathbf{u}_h \rangle \bar{e}_0) + \frac{\partial(\rho a_0 \overline{w}_0 \bar{e}_0)}{\partial z} =$$
$$\underbrace{\frac{\partial}{\partial z}\left(\rho a_0 K_{m,0} \frac{\partial \bar{e}_0}{\partial z}\right)}_{\text{turbulent transport}} + \underbrace{\rho a_0 K_{m,0}\left[\left(\frac{\partial\langle u\rangle}{\partial z}\right)^2 + \left(\frac{\partial\langle v\rangle}{\partial z}\right)^2 + \left(\frac{\partial \bar{w}_0}{\partial z}\right)^2\right]}_{\text{shear production}}$$
$$+ \sum_{i>0}\Bigg(\underbrace{-\hat{E}_{0i}\bar{e}_0}_{\text{turb. entrainment}} + \underbrace{\bar{w}_0^* \hat{E}_{0i}(\bar{w}_0 - \bar{w}_i)}_{\text{turb. entrainment production}} \Bigg)$$
$$+ \sum_{i>0}\Bigg(\underbrace{-\Delta_{0i}\bar{e}_0}_{\text{dyn. detrainment}} + \frac{1}{2}\underbrace{E_{0i}(\bar{w}_0 - \bar{w}_i)(\bar{w}_0 - \bar{w}_i)}_{\text{dyn. entrainment production}} \Bigg)$$
$$+ \underbrace{\rho a_0 \overline{w_0' b_0'}}_{\text{buoyancy production}} \underbrace{- \rho a_0 \left[\overline{u_0'\left(\frac{\partial P^\dagger}{\partial x}\right)_0'} + \overline{v_0'\left(\frac{\partial P^\dagger}{\partial y}\right)_0'} + \overline{w_0'\left(\frac{\partial P^\dagger}{\partial z}\right)_0'}\right]}_{\text{pressure work}} - \underbrace{\rho a_0 \bar{D}_{e,0}}_{\text{dissipation}}, \quad (25)$$

with TKE dissipation denoted by $\bar{D}_{e,0}$. Closure schemes for the shear production, entrainment and detrainment, turbulent transport, buoyancy production, and dissipation are discussed in Cohen et al. (2020) and Lopez-Gomez et al. (2020).

The pressure work in the environment can be computed using

$$-\rho a_0 \left[\overline{w_0'\left(\frac{\partial P^\dagger}{\partial z}\right)_0'} + \overline{u_0'\left(\frac{\partial P^\dagger}{\partial x}\right)_0'} + \overline{v_0'\left(\frac{\partial P^\dagger}{\partial y}\right)_0'}\right] = \sum_{i\geq 1} \rho a_i \left(\bar{w}_i^* - \bar{w}_0^*\right) \overline{\left(\frac{\partial P^\dagger}{\partial z}\right)}_i^*, \quad (26)$$

once the perturbation pressure gradient is closed for the momentum equations in the updrafts and downdrafts. This equation assumes that subdomain covariances within updrafts and downdrafts are negligible, a general assuption in EDMF schemes. A derivation of this relation is provided in Appendix A, given the assumption that pressure perturbations only redistribute TKE between subdomains and do no work on the grid mean (Tan et al., 2018). It is noteworthy that (26) is different from how the pressure work term is closed in many higher-order turbulence schemes (e.g., Bretherton and Park (2009)), which usually combine the pressure work with the turbulent TKE transport and parameterize the resulting combined term diffusively.

3.2 Implementation of Perturbation Pressure Closure in the Extended EDMF Scheme

Equations (14) and (20) provide the buoyancy and dynamic perturbation pressure forcing in the 2D single-normal mode flow. They apply to the pointwise vertical momentum equation within a thermal. To derive expressions similar to (14) and (20) that are suitable for implementation in the EDMF scheme, we take updrafts in the EDMF scheme to be ensembles of thermals as discussed in Appendix C, and we conditionally average over the thermals, obtaining for scalar fluxes

$$\overline{w}_i\overline{\phi}_i = \left(\frac{1}{\sum_{j=1}^N 2R_j}\right)\sum_{j=1}^N \int_{-R_j}^{R_j} w\phi d\tilde{x} = \sum_{j=1}^N \frac{a_j^T}{a_i}\left\{w\phi\right\}_j . \quad (27)$$

Here, i represents the i-th subdomain in the EDMF scheme, j represents the j-th thermal in the i-th subdomain, $\tilde{x}$ is a local coordinate centered on each thermal axis, R_j is the horizontal radius of the j-th thermal, a_j^T is the area fraction of the j-th thermal, and the $\{\cdot\}_j$ operator represents the average over the j-th thermal. In the EDMF framework, it is assumed that variance within updrafts is negligible, and the vertical transport of heat ($\overline{w_i b_i}$), or of any other tracer, is achieved through the updraft mean properties ($\overline{w}_i$ and $\overline{b}_i$), that is,

$$\frac{1}{V}\int_{\Omega_i} wb dV = \overline{w}_i\overline{b}_i. \tag{28}$$

Here, Ω_i represents the i-th subdomain within a grid box. To apply this to the thermal ensemble, the thermal-mean buoyancy (and other scalars except w) is taken as the average over the thermal, while the effective $\overline{w}_i$ is obtained from expression (28).

Applying the conditional average to the buoyancy perturbation pressure gradient as in (15), the buoyancy perturbation pressure gradient force for the i-th updraft, consisting of N thermals, is

$$-\overline{\left(\frac{\partial P_\mathrm{b}}{\partial z}\right)}_i = -\sum_{j=1}^{N}\frac{a_j^T}{a_i}\frac{1}{1+\left(\frac{H_j}{2R_j}\right)^2}\{b\}_j, \tag{29}$$

This virtual mass effect reduces the effective buoyancy of the thermal with respect to the buoyancy computed from density fluctuations (Davies-Jones, 2003; Jeevanjee & Romps, 2015). Consistent with LES simulations (Romps & Charn, 2015; Tarshish et al., 2018), the virtual mass contribution depends on the aspect ratio, $2R/H$, of the convective system.

Assuming each thermal contributes almost equally to the updraft buoyancy (i.e., $a_j^T\{b\}_j/a_i = \eta\overline{b}_i$) and that the inverse aspect ratio $\hat{\alpha} = H/2R$ of thermals ranges uniformly from 0 to a certain value $\hat{\alpha}_m$, equation (29) can be approximated as

$$-\overline{\left(\frac{\partial P_\mathrm{b}}{\partial z}\right)}_i = -\sum_{j=1}^{N}\frac{\eta\overline{b}_i}{1+\left(\frac{H_j}{2R_j}\right)^2} \approx -\frac{N}{\hat{\alpha}_m}\int_0^{\hat{\alpha}_m}\frac{1}{1+\hat{\alpha}^2}\eta\overline{b}_i d\hat{\alpha} = -\frac{N\eta}{\hat{\alpha}_m}\arctan{(\hat{\alpha}_m)}\overline{b}_i. \tag{30}$$

The $\arctan{(\hat{\alpha}_m)}$ function behaves as an activation function in terms of the maximum inverse aspect ratio $\hat{\alpha}_m$ of the thermals sustaining convection. It easily saturates (i.e., is constantly activated) for reasonable convective aspect ratios. Considering the steeper part of the $\arctan{(\hat{\alpha}_m)}$ function might be important for high spatial resolutions, where there are fewer thermals within a grid box. In the EDMF implementation, we use expression (30) to diagnose the departure from the grid mean following (24).

The implementation of the dynamic perturbation pressure gradient in the EDMF scheme requires an effective vertical velocity $\bar{w}_i$, defined by (28). Consider a simplified case with a single thermal and let $w_c(z) = w_A\sin{(mz)}$ and $b_c(z) = b_A\sin{(mz)}$ represent the vertical velocity and buoyancy at the thermal axis. Following (28),

$$\overline{w}_i\overline{b}_i = \frac{1}{2R}\int_{-R}^{R} w_c\cos{(2k_b x)} b_c\cos{(k_b x)}dx = \frac{2}{3\pi}w_c b_c, \tag{31}$$

and thus the updraft velocity $\overline{w}_i$ is proportional to the vertical velocity at the axis of the thermal when considering one thermal. Writing $\overline{w}_i^* = \gamma w_{c,j}$, applying the conditional average on the advection damping term in (20), and diagnosing the pressure drag from the pressure deficit across the thermal ensemble yields the dynamic perturbation pressure gradient for the updraft

$$-\overline{\left(\frac{\partial P_\mathrm{d}}{\partial z}\right)}_i^* = \frac{1}{\gamma^2}\overline{w}_i^*\frac{d\overline{w}_i^*}{dz} - \frac{1}{2}c_d\frac{w_{r,i}^2}{H_i} = \alpha_a\overline{w}_i^*\frac{d\overline{w}_i^*}{dz} - \frac{1}{2}c_d\frac{w_{r,i}^2}{H_i}. \tag{32}$$

The first term on the right-hand side counteracts the advection of vertical momentum in (23). The parameter $\alpha_a = \gamma^{-2}$ is a scaling parameter that describes the advection damping strength. This term stands out as the only term that can serve as a source of momentum in a buoyant thermal bubble; the resulting acceleration in the lower half of the bubble is an important term in the vertical momentum budget. It is tightly connected to the vertical structure of P_{d}, as indicated by the first term on the right-hand side of (17). The dynamic perturbation pressure attributed to this term has high pressure centered at the top and bottom of the thermal and low pressure centered at the thermal center, consistent with the dynamic pressure structure from numerical simulations of an idealized thermal bubble (Peters, 2016; Morrison & Peters, 2018) and the multi-mode ensemble of thermal structures as shown in Figure C1.

By contrast, the simplification via the single-normal mode ansatz leads to a vertically symmetric structure with respect to the thermal center (similar to Hill's vortex), whereas the numerical simulations in Morrison and Peters (2018) demonstrate some asymmetry. As discussed in Peters (2016), the high pressure at the top and bottom is related to the $-(\partial_x u)^2 - (\partial_z w)^2$ term in the Poisson equation (4), and it partially compensates the divergence of the flow. The low pressure in the center is related to the $-(\partial_z u)\partial_x w$ term in the Poisson equation and comes from the vortex ring-like structure. This high-low-high vertical pattern leads to an upward pressure gradient force in the lower half of the thermal and a downward force in the upper half, counteracting the momentum advection in the $\overline{w}_i$ prognostic equation.

The second term in (32) represents a form drag, a necessary correction to the simplified configuration given by free-slip boundary conditions between thermals and the environment. In the EDMF scheme, a z-dependent relative velocity is computed as $w_{r,i} = \overline{w}_i - \overline{w}_0$, and thus, the drag term is defined as

$$-\alpha_d \frac{(\overline{w}_i^* - \overline{w}_0^*)|\overline{w}_i^* - \overline{w}_0^*|}{H_i}, \tag{33}$$

where the subscript i represents the i-th updraft/downdraft and 0 represents the environment. The velocity $\overline{w}_i^* - \overline{w}_0^*$ is the relative velocity between the updraft/downdraft and the environment (with the grid mean $\langle w \rangle$ removed from both $\overline{w}_i$ and $\overline{w}_0$). For simplicity, the factor 1/2 in the derivations of the drag is subsumed into the parameter α_d, which we later adjust empirically. Note that the squared velocity has been substituted by a product with its absolute value, consistent with the fact that for a downdraft the total pressure difference between $z = H$ and $z = 0$ has opposite sign.

The drag term (33) is different from commonly adopted drag terms (e.g., Simpson and Wiggert (1969); de Roode et al. (2012); Tan et al. (2018)) in two respects: First, it uses the relative velocity between the drafts and the environment instead of the updraft velocity, which is applicable for large updraft area fractions; second, it uses a $1/H$ scaling instead of the $1/R$ scaling, which we found to be crucial for the diurnal cycle of deep convection.

As shown in Appendix B, for the axisymmetric thermal, contributions to the perturbation pressure gradient can also be decomposed into virtual mass, advection damping, and drag, with the main difference being the scaling parameters that arise. Therefore, the pressure gradient force for the i-th EDMF subdomain can be generalized as

$$-\overline{\left(\frac{\partial P^\dagger}{\partial z}\right)}_i^* = -\alpha_b \bar{b}_i^* + \alpha_a \bar{w}_i^* \frac{\partial \bar{w}_i^*}{\partial z} - \alpha_d \frac{(\bar{w}_i^* - \bar{w}_0^*)\,|\bar{w}_i^* - \bar{w}_0^*|}{\min\left(H_i, 500 \text{ m}\right)}, \tag{34}$$

where α_b, α_a, and α_d are dimensionless parameters that describe the contributions from the virtual mass effect, advection damping, and pressure drag. A minimum length scale of 500 m is used to avoid a vanishing denominator. In the examples we show, we tuned these parameters manually for the scheme to perform across a spectrum of convective scenarios. A significant change in the drag formula is that the vertical extent of the convective system rather than the horizontal radius (as in Tan et al. (2018) or Simpson et al. (1965)) is used as the length scale. It is shown in Section 5 that this is a key modification that allows the EDMF scheme to correctly capture the onset of deep convection.

The pressure formulation (34) has three tunable, non-dimensional parameters: a virtual mass parameter (α_b), an advectivon damping parameter (α_a), and a drag parameter (α_d) (in addition to the cutoff length scale). The virtual mass parameter (α_b) is dependent on the number and aspect ratio of thermals sustaining convection, but Eq. (30) suggests it assumes an approximately fixed value when the number of thermals is large. The advection damping parameter (α_a) describes a compensation between perturbation pressure gradient and the momentum advection so that the flow stays non-divergent. The drag parameter (α_d) modulates the strength of the drag effect. Romps and Charn (2015) determined the drag coefficient for a spherical thermal to be 0.6. Tan et al. (2018) took into account this drag formula and adjusted the coefficient for the spherical thermal to that of a cylindrical plume. However, the drag effect as in Romps and Charn (2015) did not separate the buoyancy and dynamic contributions. Their drag term represents the entire pressure gradient force, which is conceptually different from the drag term we derived in (34).

While the three parameters have direct physical interpretations, we take them as empirical parameters to be learned from data. The parameters ($\alpha_b, \alpha_a, \alpha_d$) are a subset of the EDMF parameters, which we obtained sequentially: We first tuned the mixing length parameters with stable boundary layer simulations (Lopez-Gomez et al., 2020), followed by the entrainment parameters and (α_b, α_a) parameters relevant to dry convection (Cohen et al., 2020). Finally, we tuned the moisture-dependent detrainment parameters and the drag coefficient α_d to reproduce the cloud layer profiles and the cloud top height in moist convection.

4 Experimental Setups in LES and SCM

We implemented the extended EDMF framework in the SCM described in Tan et al. (2018) and Cohen et al. (2020). It uses the liquid potential temperature (θ_l) as the prognostic thermodynamic variable for both dry and moist experiments. For dry cases, $\theta_l = \theta$. We take (34) as the pressure closure for the updraft vertical momentum equation and (26) as the pressure work for the environmental TKE equation. The performance of the EDMF scheme in the SCM is compared with LES. The LES are performed with PyCLES (Pressel et al., 2015), an anelastic atmospheric LES code with entropy and total water specific humidity as prognostic variables, designed to simulate boundary layer turbulence and convection. We examine the structure of a dry rising bubble following the benchmark test in Bryan and Fritsch (2002), and also compare our simplified thermal bubble structure to individually selected thermals in observationally motivated test cases of moist convection.

4.1 2D Dry Rising Bubble

4.1.1 LES Setup

The dry rising bubble experiment runs on a 2D domain of 10 km in height and 20 km in width. The initial liquid water potential temperature (θ_l) distribution over the domain is

$$\theta_l(x,z) = \begin{cases} 300\text{ K} + (2\text{ K})\cos^2\left(0.5\pi L(x,z)\right), & \text{if } L < 1, \\ 300\text{ K}, & \text{if } L \geq 1, \end{cases} \tag{35}$$

where

$$L = \sqrt{\left(\frac{x - x_c}{x_r}\right)^2 + \left(\frac{z - z_c}{z_r}\right)^2} \tag{36}$$

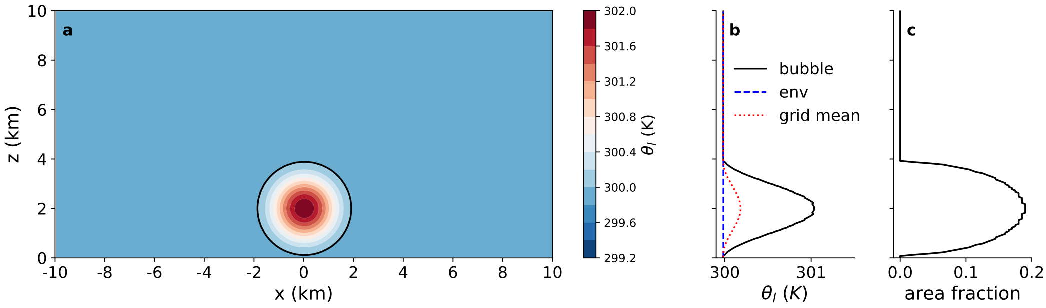

Figure 2. Initial profiles of the rising bubble experiments in LES. (a) Contours of θ_l with intervals of 0.2 K. The black contour is at 300 K and it outlines the edge of the initial bubble that is used for the conditional average computation. (b) Initial vertical profiles of θ_l conditionally averaged over the bubble (black solid line) and the environment (blue dashed line), as well as the grid-mean θ_l (red dotted line). (c) Initial profile of the bubble area fraction.

represents the normalized distance from the point (x, z) to the bubble center $x_c = 10$ km and $z_c = 2$ km, and $x_r = z_r = 2$ km represent the initial radius of the bubble. This initial θ_l distribution is unstable near x_c and stable far from it (Figure 2a). The thermal bubble contains the strongest warm anomaly in the bubble center, which decays toward the edge of the bubble. The liquid water potential temperature θ_l is homogeneous outside the bubble, creating an almost neutral environment. Both the environment and the bubble are initially at rest. The buoyancy force associated with the perturbed θ_l field provides the initial momentum source for the bubble to rise.

4.1.2 SCM Setup

The SCM simulation is initialized by taking the conditional average over the bubble from the LES initial setup. The buoyant bubble is identified by the 300-K θ_l-contour (black contour in Figure 2a). The initial updraft area fraction is computed as the ratio of the horizontal extent of the bubble over the horizontal LES domain size as shown in Figure 2c. Initial θ_l for the updraft is computed as the conditional average of θ_l within the perturbed area, shown in Figure 2b. Also shown are the grid-mean and environmental profiles of initial θ_l. This initial θ_l profile introduces a positively buoyant bubble into a negatively buoyant environment. The updraft velocity is initialized as zero throughout the column, consistent with the resting initial state in LES. No external forcing is applied along the simulation.

As discussed in Cohen et al. (2020), subdomain horizontal velocities are assumed equal to the grid-mean horizontal velocity, and changes in area fraction due to horizontal mass exchange are attributed to dynamical entrainment and detrainment. A rising bubble results in a large mass and momentum convergence at the bubble bottom and divergence at the top (Sánchez et al., 1989). This requires an additional divergence term in addition to the dynamical entrainment and detrainment. Therefore, the entrainment and detrainment rates for the bubble test case are modified as

$$E_{ij} = \tilde{E}_{ij} + \rho c_{\mathrm{div}} \max\left(\frac{\mathrm{d}(a_i w_i)}{\mathrm{d}z}, 0\right), \tag{37}$$

$$\Delta_{ij} = \tilde{\Delta}_{ij} + \rho c_{\mathrm{div}} \max\left(-\frac{\mathrm{d}(a_i w_i)}{\mathrm{d}z}, 0\right), \tag{38}$$

where $c_{\rm div} = 0.4$ is a scaling coefficient, and $\tilde{E}_{ij}$ and $\tilde{\Delta}_{ij}$ are the entrainment and detrainment rates proposed by Cohen et al. (2020). The second term is an addition for the bubble test case only; it has been implemented in an EDMF scheme for simulating oceanic convection (Giordani et al., 2020) and a multi-fluid framework for the thermal bubble (Weller et al., 2020). The bubble test case is an initial value problem that is different from the typical boundary value problems for turbulence and convection that a SGS model needs to simulate in a climate model, and hence the introduction of these additional terms, not present in Cohen et al. (2020) and Lopez-Gomez et al. (2020), may be justified. The parameters for the pressure gradient force (34) for the 2D thermal bubble simulation are set to $(\alpha_b, \alpha_a, \alpha_d) = (0.14, 0.4, 0.1)$.

4.2 Moist Convection

Atmospheric convective systems consist of large numbers of thermal bubbles (Moser & Lasher-Trapp, 2017; Hernandez-Deckers & Sherwood, 2016), which can be identified by their dynamical and thermodynamic properties (e.g., Romps and Charn (2015)). Morrison et al. (2020) and Peters et al. (2020) illustrate a more complicated thermal chain structure under certain conditions that links the convective updrafts to starting plumes. A convective parameterization attempts to represent the statistical mean of these bubbles.

We have already shown the EDMF scheme with the proposed pressure closure to be successful in representing various boundary layer regimes, including stratocumulus-topped boundary layers, dry convective boundary layers, and shallow and deep moist convection (Cohen et al., 2020; Lopez-Gomez et al., 2020). Here we present the following two moist convective cases, in which the perturbation pressure gradient is an important forcing term:

- A maritime shallow convection case from the Barbados Oceanographic and Meteorological Experiment (BOMEX, Holland and Rasmusson (1973)). The initial profile and large-scale forcing follow the experiment specifications in Siebesma et al. (2003). We use a $(6.4\ \text{km})^2 \times 3$ km domain with an isotropic resolution of 40 m.
- A continental deep convection case from the Tropical Rainfall Measurement Mission Large-scale Biosphere-Atmosphere experiment (TRMM-LBA, Grabowski et al. (2006)). The initial profile and time-evolving surface fluxes follows the experiment specifications in Grabowski et al. (2006). A warm-rain cutoff scheme is implemented consistently in both LES and SCM. The simulation runs on a $(25.6\ \text{km})^2 \times$ 22 km domain with an isotropic resolution of 200 m.

The LES and SCM simulations for BOMEX and TRMM-LBA follow the experimental setups described in Cohen et al. (2020). The pressure closure takes the form (34) with parameters $(\alpha_b, \alpha_a, \alpha_d) = (0.12, 0.1, 10.0)$. (We use different parameters for 2D and 3D cases, as suggested by the derivations in Section 2 and Appendix B.) The closures for entrainment and detrainment are given by Eqs. (31) and (32) in Cohen et al. (2020), that is, without the divergence term as described above for the bubble case. The eddy diffusivity and mixing length in the environment are closed as in Lopez-Gomez et al. (2020). At the same time, the results in these companion papers rely on the pressure closure derived in this work.

Following Couvreux et al. (2010), a passive tracer is added for the LES simulation. A 3D mask that identifies updrafts in moist convection is obtained based on criteria on the vertical velocity, tracer concentration, and liquid water specific humidity as described in Cohen et al. (2020). We compute the bulk properties of convective plumes by taking the conditional average over the updraft mask. Against these bulk properties, we compare the performance of the updraft profiles in the SCM simulations.

To investigate the average structure of thermal bubbles in moist convection, we identify bubbles from the 3D outputs for the last simulation timestep. We search for thermals as coherent subsets of the updraft structures. To exclude negatively buoyant structures, which can occur near cloud top in convective overshoots, we remove regions of negative buoyancy from the tracer-based updraft identification.

In BOMEX, thermal bubbles are identified by sweeping over the 3D fields from the cloud-top level down to cloud-base. For TRMM-LBA, we perform a top-down search for convective thermals that grow above 3 km. The 3D mask that identifies updrafts in fact labels isolated clusters that sit at different horizontal and vertical locations of the simulation domain. At each height level, once a cluster (2D) with at least 3 neighboring grid cells is located via the updraft identification criteria, this cluster becomes a candidate to be part of the thermal. Further down in the computational domain, when 2D clusters identified in a lower level overlap with the clusters identified above, then they are considered to be part of the same 3D thermal. Once such 3D thermal elements have been identified, those with horizontal or vertical scales smaller than 5 grid cells are excluded from the analysis, to avoid randomness from small structures. In the end, we identify 13 convective thermals from BOMEX and 8 from TRMM-LBA for a composite study. Various more complicated thermal tracking algorithms are available (e.g., (Romps & Charn, 2015; Hernandez-Deckers & Sherwood, 2016; Morrison et al., 2021)). These take into consideration flow structures and their time evolution and investigate the time-evolving characteristics of the thermals. This is beyond the scope of this work. Our aim merely is to compare our solution for the perturbation pressure against thermals in LES snapshots.

A composite of the thermal bubbles is created to illustrate their robust structures in w, buoyancy, $P^\dagger$ and $-\partial_z P^\dagger$. First, for each bubble, the location of the maximum w is identified as the reference grid point for the composite analysis. Then, an azimuthal average is computed around the vertical axis that goes through the location of the maximum w in the bubble. Finally, the composite is created by aligning the 2D azimuthal averages of each bubble by their locations of maximum w.

5 Results

5.1 2D Rising Bubble

Snapshots of the bubble structure from LES are shown in Figure 3. Similar to Figure 2a, the bubble is outlined by black contours with zero buoyancy. Given this initial buoyancy distribution, the upward vertical velocity builds up quickly inside the bubble, while compensating downdrafts are established and closely wrap the rising bubble. This is a robust structure in convective elements and captures well the vertical fluxes of heat and moisture in convective systems (Gu et al., 2020). Meanwhile, a negative perturbation pressure is established below the maximum buoyancy level, while a positive perturbation pressure is established above it. As the buoyancy center is pushed upward as the bubble rises, the zero perturbation pressure contour line moves toward the bubble top, and negative $P^\dagger$ dominates the majority of the bubble. A peak in negative $P^\dagger$ develops at the center of the bubble, which results in a momentum source from the perturbation pressure gradient below this level and a momentum sink above it. The bottom panels in Figure 3 show the conditional average of the pressure gradient force and its decomposition into buoyancy and dynamic components. At the bottom and mid-levels of the bubble, $-\partial_z P_{\mathrm{d}}^\dagger$ dominates; it is a momentum source in the lower part of the bubble and a sink near its top. The buoyancy component, $-\partial_z P_{\mathrm{b}}^\dagger$, contributes primarily as a sink offsetting the buoyancy field.

During the early stages of the simulation (before 600 s), the 2D structure of the buoyancy and velocity fields resembles the trigonometric structure assumed in (6) and (7). Therefore, the single-normal mode assumption is a reasonable simplification. The

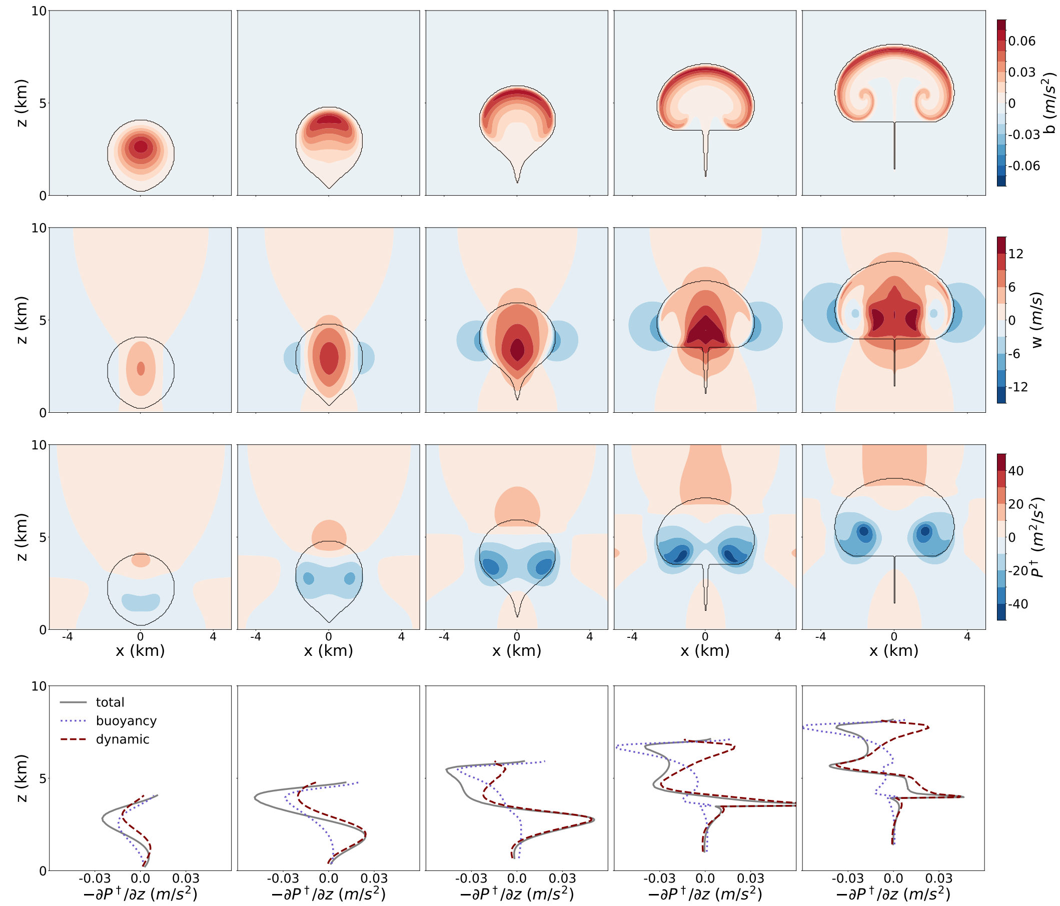

Figure 3. Snapshots of the rising bubble in 200-second intervals. The black contour in each contour plot traces the bubble boundary. From left to right are bubbles at 200, 400, 600, 800, and 1000 seconds into the simulation. The first 3 rows from top to bottom are buoyancy, vertical velocity, and perturbation pressure potential $P^\dagger$. The bottom row shows conditional averages of the perturbation pressure gradient force $-\partial_z P^\dagger$ and its decomposition into the buoyancy and dynamic components.

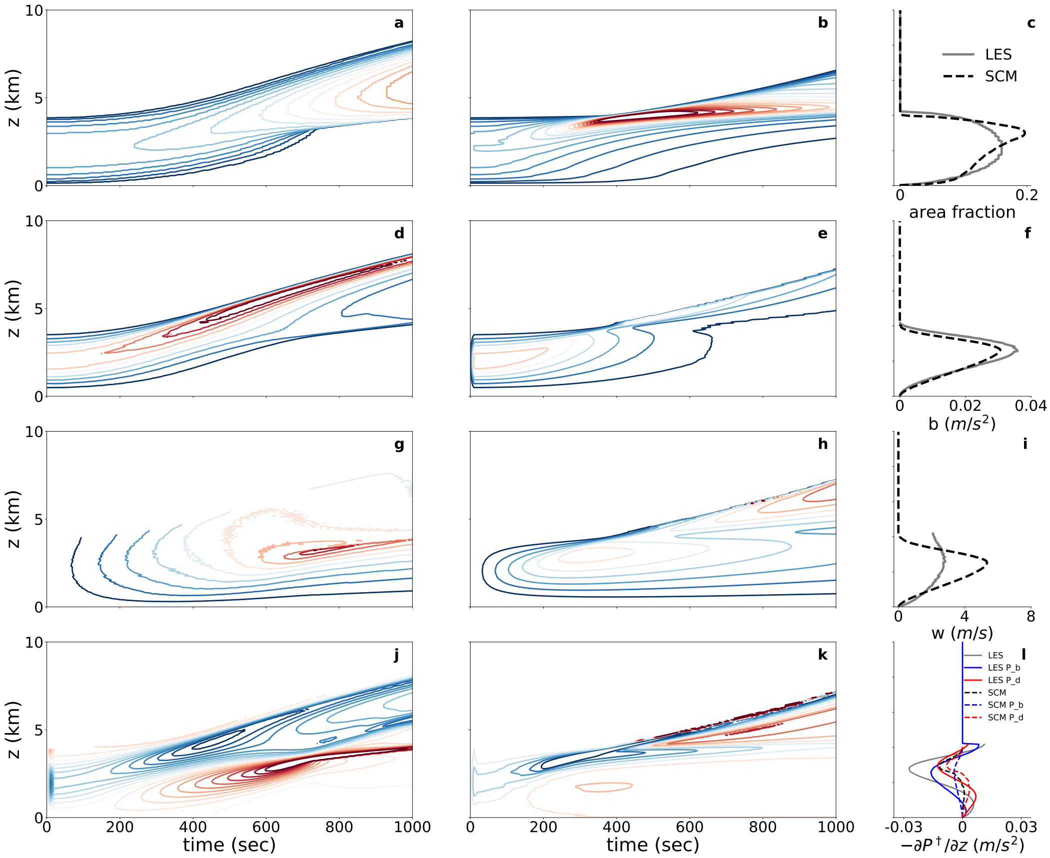

Figure 4. Comparison of bubble structures between LES and SCM simulations. (a) Time evolution of the bubble area fraction in LES. Contours from blue to red represent [0.06, 0.08, . . . , 0.30]. (b) Time evolution of the bubble area fraction in SCM. Contours from blue to red represent [0.06, 0.08, . . . , 0.40]. (c) Vertical profiles of area fraction for the 200-second step of the LES (solid) and SCM (dashed) simulations. (d) Time evolution of the bubble buoyancy in LES. Contours from blue to red represent [0.005, 0.010, . . . , 0.045] m s^{-2}. (e) Time evolution of the bubble buoyancy in SCM. Contours from blue to red represent [0.005, 0.010, ..., 0.030] m s^{-2}. (f) As in(c) but for buoyancy. (g) Time evolution of the bubble vertical velocity in LES. Contours from blue to red represent [1, 2, ..., 9] m s^{-1}. (h) Time evolution of the bubble vertical velocity in SCM. Contours from blue to red represent [1, 2, ..., 8] m s^{-1}. (i) As in (c) but for vertical velocity. (j) Time evolution of the bubble $-\partial_z P^\dagger$ in LES. Contours from blue to red represent [-0.05, -0.045, ..., 0.045] m s^{-2}. (k) Time evolution of the bubble $-\partial_z P^\dagger$ in SCM. Contours from blue to red represent [-0.01, -0.008, ..., 0.01] m s^{-2}. (l) As in (c) but for $-\partial_z P^\dagger$ and its decomposition into the buoyancy and dynamic contributions.

perturbation pressure exhibits a dumbbell structure in the lower part of the bubble, which indicates the dynamic perturbation pressure associated with velocity plays an essential role at these levels. Toward the end of the simulation, when the bubble deforms, the flow inside the bubble deviates from the single-normal mode structure as the strong buoyancy is pushed to the bubble's top while the maximum vertical velocity falls into the lower half of the bubble. However, a close investigation of the moist convective cases in the next subsection shows that individual bubbles in the convective system resemble the rising bubble structures during the early stages, which validates the single-normal mode assumption made in the derivation.

The SCM with the extended EDMF parameterization and the pressure closure simulates the time evolution of the rising thermal bubble well, with greater success at early stages, as shown in Figure 4. The time evolution shows a rising bubble that for the most part detaches from the surface and maintains a coherent buoyancy anomaly. As the bubble rises, the maximum buoyancy level in the SCM simulation shifts from the bubble's center to its top, in agreement with the LES results. The area fraction shows a slightly sharper gradient at the top of the bubble at around 400 s. The SCM also roughly captures the vertical velocity evolution in the LES. Throughout the simulation, the perturbation pressure gradient acts as important momentum source (see Figure 4j and 4k). However, after 600 s in the simulation, the pressure gradient force's contribution as momentum source stays at the lower half of the bubble in the LES but is pushed toward the bubble top in the SCM. This mismatch is a result of the discrepancies in w profiles in the later stages of the simulation, where the single-normal mode ansatz is no longer valid.

The last column of Figure 4 shows the profiles at 200 s simulation time, when the bubble has in a roughly symmetric structure and a single-normal mode is a reasonable assumption. The SCM reproduces the buoyancy profile from the LES, although it overestimates the area fraction toward the bubble top and the vertical velocity throughout. In spite of these differences, the SCM produces a bubble that has many key features in the LES simulation. The $-\overline{(\partial P^\dagger/\partial z)}_i$ profile in the SCM contributes to a slight momentum source in the lower half of the bubble and a momentum sink in the upper half, as expected from the LES diagnostics. However, the magnitude of the pressure gradient force in the SCM is smaller than in the LES. A decomposition into the dynamic and buoyancy perturbation pressure contributions shows that the buoyancy perturbation contribution is smaller than expected from LES. Considering the well-reproduced buoyancy profile, the underestimate of the buoyancy perturbation pressure gradient is mainly due to $\alpha_b = 0.14$ being too small. Since the bubble at 200 s has similar horizontal and vertical extents, the single-normal mode yields $\alpha_b \approx 0.5$. However, this constitutes too much inhibition and prevents the bubble from rising in the SCM setting. Despite the discrepancies in magnitude, the perturbation pressure gradient closure captures the primary physics of the perturbation pressure, i.e., the maintenance of a non-divergent flow. Overall, this demonstrates the capability of the EDMF framework with the pressure closure to simulate a rising bubble.

5.2 Moist Convection

Thermal bubbles identified from the BOMEX and TRMM-LBA LES experiments demonstrate structures similar to the early stage of the rising thermal bubble experiment. Figure 5 shows the vertical velocity, buoyancy, perturbation pressure potential, and $-\partial_z P^\dagger$ profiles for a composite of bubbles selected in the BOMEX and TRMM-LBA test cases. The buoyancy profiles resemble those of early-stage bubbles. The perturbation pressure fields show the clear pattern of low pressure in the middle and lower levels of the bubble and high pressure at the top. The dumbbell structure characterizing the later stages of the rising bubble experiment does not show up in the composite (averaged) fields in Figure 5; however, it does show up if one looks at individual bubbles instead of the composite. They are smoothed out when averaged over several bubbles with various hori-

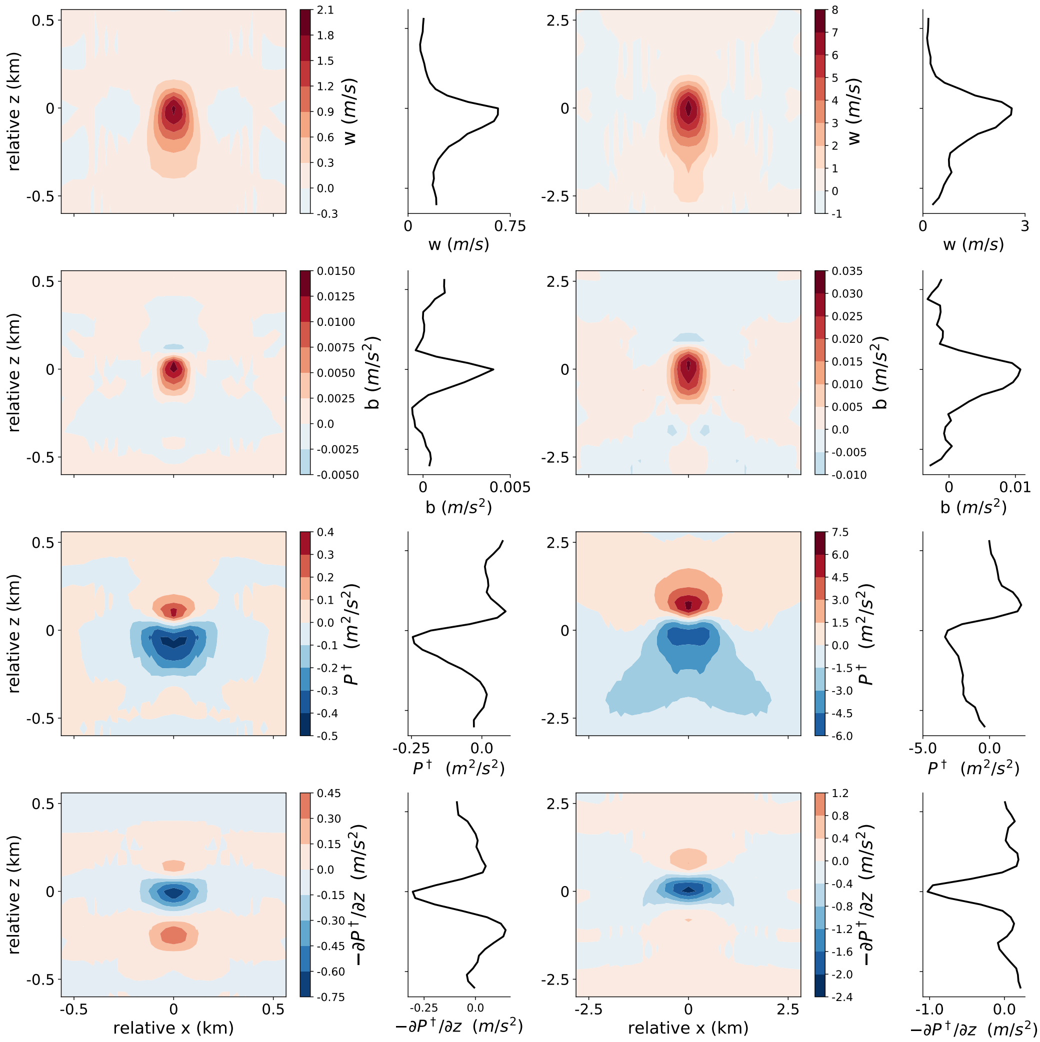

Figure 5. Average structures of bubble composites identified from LES simulations for BOMEX (left two columns) and TRMM-LBA (right two columns). Contour plots represent the azimuthally averaged structures of w, buoyancy, $P^\dagger$, and $-\partial_z P^\dagger$. The x and y axis in the contour plots represent the relative distances from the location of maximum vertical velocity. Column 2 (BOMEX) and 4 (TRMM-LBA) show the horizontal average of the bubble properties. Rows from top to bottom show vertical velocity, buoyancy, $P^\dagger$, and $-\partial_z P^\dagger$.

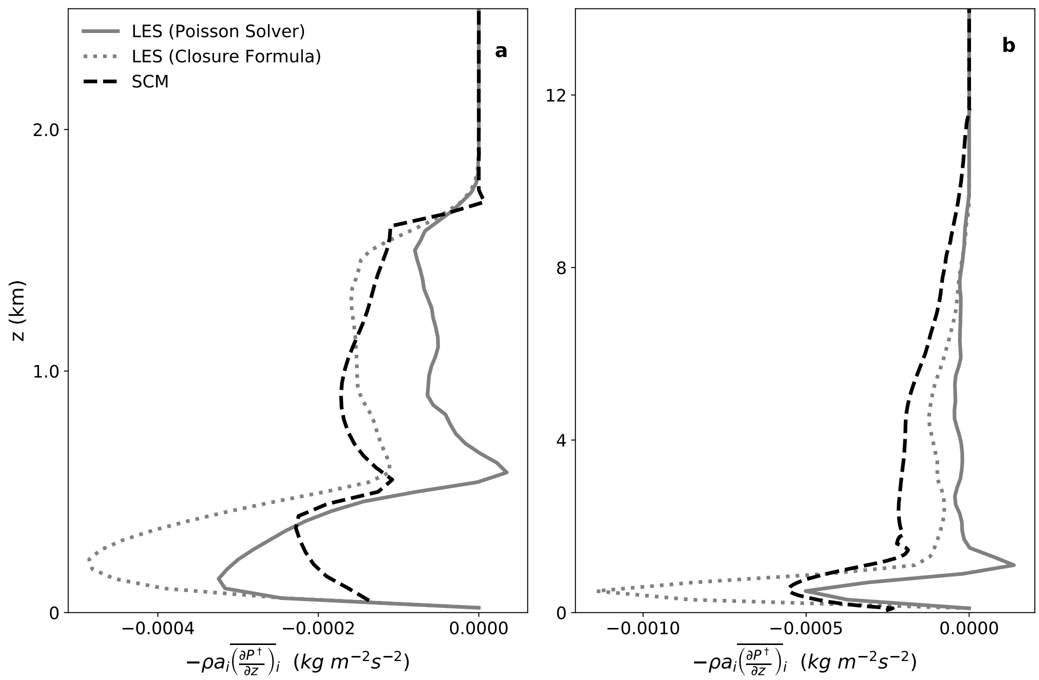

Figure 6. Comparison of $-\rho a_i \overline{(\partial P^\dagger/\partial z)_i}$ between LES and SCM for BOMEX (left) and TRMM-LBA (right). Pressure in the LES is shown in the grey solid line; pressure diagnosed from LES using (34) is shown in the grey dotted line; pressure from SCM is shown in the black dashed line.

zontal and vertical extents. Averaged over many bubbles, the momentum source from $-\partial_z P^\dagger$ at the bottom of the bubble and the sink at the top remain similar to the structure found in the rising bubble experiment.

The vertical velocity profiles show a much stronger asymmetry between upward and downward flow, compared to both the bubble experiment and the single-normal mode ansatz shown in Figure 1. This, however, is predicted by the single-normal mode solution when averaging over thermals with different horizontal scales, as shown in Figure C1. Indeed, all fields in Figure 5 show a structure similar to that predicted by an ensemble of single-normal mode thermals. The resemblance between the composite of bubbles from moist convection and the multi-mode ensemble (Figure C1) justifies the implementation of the proposed perturbation pressure closure in the EDMF framework. The analytical structure for the multi-thermal ensemble as shown in Figure C1 is also consistent with the idealized simulation results of Morrison (2016b).

Using the pressure closure described here, Cohen et al. (2020) demonstrate the capability of the EDMF framework to represent dynamic and thermodynamic properties within the updrafts, as well as their first, second, and third moments. Here we focus on the performance of the pressure closure (34) in the BOMEX and TRMM-LBA cases through comparison between the LES and SCM simulations (Figure 6). Comparing the profiles for the vertical pressure gradient force in the SCM (dashed) with that diagnosed from (34) in LES (dotted), the SCM pressure closure captures the LES vertical profile well in the BOMEX case. For the TRMM-LBA case, the pressure gradient profile in the SCM represents a much larger momentum sink above the boundary layer compared to the LES.

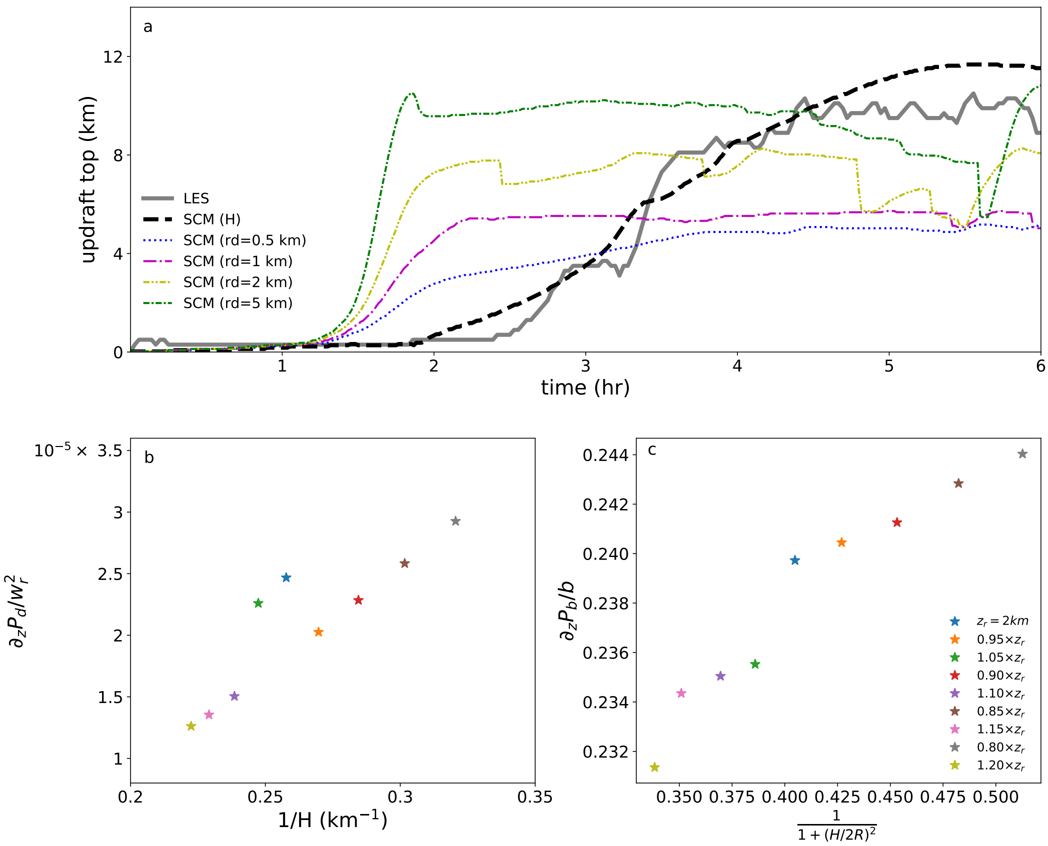

Figure 7. (a) Comparisons of the TRMM-LBA cloud top evolution between LES (grey solid line) and SCM simulations with different pressure drag closures. SCM results with updraft height as length scale, as given by (32), are shown in the black dashed line. SCM results with characteristic plume radius as length scale in the pressure drag, as given by (39), are shown in the colored dashed lines for different values of r_d. (b) $-\overline{(\partial P_d/\partial z)}/w_r^2$ versus $1/H$ where H is the vertical extent of the bubble in thermal bubble test case, the overbar represents a bubble average, and w_r is the ascent velocity of bubble measured at the bubble top. (c) $\overline{(\partial P_b/\partial z)}/\overline{b}$ versus $(1+(H/2R)^2)^{-1}$ where H and R are the vertical and horizontal extents of the bubble and b is the buoyancy.

This is primarily due to a discrepancy of the buoyancy profile between the SCM and LES results, which leads to a larger sink from the buoyancy perturbation pressure component.

The EDMF framework represents the heat transport by the mass flux of the coherent updraft $\overline{w}_i$ and the updraft buoyancy $\overline{b}_i$ (neglecting the variance within each updraft) and the diffusive flux in the turbulent environment. Cohen et al. (2020) demonstrate a well matched mass-flux profile and $\langle w^*\theta^*\rangle$ profile at the expense of accurate individual profiles of $\overline{w}_i$ and $\overline{b}_i$. Comparing the pressure gradient profiles as diagnosed from (34) (dotted) with that solved from the LES (solid), the former is about twice the magnitude of the latter. This is due to a considerable drag effect ($\alpha_d = 10.0$). The large drag effect is needed as a stabilization requirement (Weller & McIntyre, 2019). Unlike for the buoyant bubble, the pressure gradient force for the bulk updrafts in BOMEX and TRMM-LBA acts primarily as a momentum sink throughout the column, except at the cloud base.

6 Discussion

An advantage of the current pressure closure manifests itself when examining the diurnal cycle of deep convection in SCM simulations and LES. Simulating the diurnal cycle is a major challenge for many parameterization schemes (Dai & Trenberth, 2004; Holtslag et al., 2013). Here we show the effect of the length scale used in the denominator of the pressure drag on the timing of deep convection. When using a fixed scale, e.g., the updraft radius (Simpson & Wiggert, 1969; Tan et al., 2018), a trade-off arises between improving the onset timing of convection and improving the cloud top height. In Tan et al. (2018), the pressure drag term in the i-th subdomain was written as

$$-\overline{\left(\frac{\partial P_d^\dagger}{\partial z}\right)_i}^{*} = -\alpha_d \frac{(\bar{w}_i^* - \bar{w}_0^*)|\bar{w}_i^* - \bar{w}_0^*|}{r_d\sqrt{a_i}}, \tag{39}$$

where $r_d = 500$ m is the typical distance between neighboring plumes in shallow convection; thus, $r_d\sqrt{a_i}$ gives a characteristic plume radius. Our derivation indicates that the drag effect scales with the vertical scale of the convective system. Figure 7 compares the evolution of updraft tops in SCM and LES for the TRMM-LBA case. The SCM simulations have fixed coefficients $\alpha_b = 0.12$ and $\alpha_a = 0.1$. We compare the drag term in closure (34) with expression (39) as in Tan et al. (2018). The value $r_d = 500$ m reproduces shallow convection as in Tan et al. (2018), but it leads to too early onset and too low updraft tops for the deep convective case. A simple increase in r_d results in a universal decrease in the drag contribution and produces higher updraft tops. However, this does not solve the problem of the onset timing. Physically, convection in the TRMM-LBA case requires a large drag in the early stages, so that convection is not initiated too early, and a gradually decreasing drag later, so that convection can grow high enough. The height of the updraft top, which arises in the normal mode derivation above, is therefore a natural scale. The timing of the onset and the height of the updraft are both substantially improved when using the updraft height as a length scale. The same value of α_d can be used for both shallow and deep convection.

The usefulness of the formulations derived from the single-normal mode approximation is also evident in the rising bubble simulations. We performed a simple sensitivity test by varying the vertical extent of the bubble (z_r) by factors ranging from 0.80 to 1.20, with intervals of 0.05. We computed mean thermal averages of all properties (e.g., the decomposed pressure gradient force, buoyancy, etc.) for the first 200 s of each simulations. Figure 7b and 7c show the H^{-1} scaling for the dynamic pressure gradient and the $(1+(H/2R)^2)^{-1}$ for the virtual mass effect. This is consistent with previous analyses of distinct thermals in convection (e.g., Romps and Charn (2015)).

We use the vertical scale H of the updraft as the length scale for the drag term. In the buoyancy and the momentum advection terms, it appears in the aspect ratio, $H/(2R)$, as a parameter characterizing the shape of the thermal. The parameters for the buoyancy and advection terms show a complicated dependency on the shape of the thermal: Changing from the 2D box pattern described by trigonometric functions to the 3D axisymmetric pattern described by Bessel functions, a scaling coefficient is needed in modifying the aspect ratio in the formula. Thus, for a more realistic structure, we anticipate a more complicated modification will be needed. Instead of seeking the complicated dependencies on the dimensionless aspect ratio, we make the coefficient for buoyancy empirical and learn it from data.

The LES show that the perturbation pressure gradient force is a momentum source in the lower half of the bubble and near cloud base levels in moist convection, which ensures the non-divergence property. This can be achieved only through the advection damping term. However, its contribution in SCM settings is not as prominent as expected from LES diagnostics. In fact, the pair of parameters for the advection damping and the drag terms indicates their relative importance in the dynamic pressure gradient. In the moist convection experiments, the parameter combination $(\alpha_a, \alpha_d) = (0.1, 10.0)$ implies a negligible contribution from the advection damping term. In the rising bubble experiment, by contrast, the advection damping contributes as an important source (Figure 3l) but with smaller magnitude compared with the LES results. In fact, the parameterization scheme contains multiple closure formula. With a proper choice of other parameters, one can manage to run the simulation successfully even without the advection damping term. Despite its small contribution as indicated by $\alpha_a = 0.1$, we retain this term in the closure formula because it represents essential physics. The current parameter sets used here and in the other two companion EDMF papers (Cohen et al., 2020; Lopez-Gomez et al., 2020) are obtained through a sequential optimization processes with a limited set of cases. We expect to obtain better insights into the parameters with advanced parameter learning techniques (Schneider et al., 2017; Cleary et al., 2021) and enlarged datasets (e.g., generated as proposed in Shen et al. (2020)); this is reserved for future work.

There has been a continuous discussion of the plume-vs-thermal viewpoint for the representation of convective systems (Levine, 1959; Simpson et al., 1965; Yano, 2014; Morrison et al., 2020). Recent studies identify criteria (i.e., updraft width, environmental relative humidity, and available potential energy) for the transition between plume-like updrafts, thermal-like updrafts, and more complicated updraft structures consisting of successive thermals. It has been shown that the updraft structure impacts the patterns for the perturbation pressure (Morrison & Peters, 2018; Peters, 2016). Although the solution derived here is based on the diagnostic Poisson equation and follows from the single-normal mode ansatz for buoyancy and velocity, the updraft structure influences the spatial structure of the perturbation pressure. The EDMF scheme represents the SGS processes inside a grid cell by a turbulent environment and coherent updrafts. We view the updrafts as ensembles of discrete thermal bubbles with varying spatial scales and model their ensemble effect with the normal mode assumption.

7 Conclusion

We have derived an analytical formula for the perturbation pressure for convective systems under the assumption of a single-normal mode for individual thermals in a Boussinesq fluid. Large-eddy simulations show that the normal mode assumption is justified both for an idealized thermal bubble and for a composite average over thermal bubbles in moist convection. This perturbation pressure formula is essential to make the extended EDMF framework a unified parameterization for turbulence and convection across a range dynamical regimes. Specifically the pressure closure proposed here plays a key role in unifying both shallow and deep convection in a single model. Moreover, the extended EDMF framework with this pressure closure reproduces a dry rising bubble benchmark—an initial value problem rather than a boundary value problem—that can be consistently simulated only in time dependent parameterizations (Tan et al., 2018; Thuburn et al., 2018; Weller et al., 2020).

The pressure closure derived here consists of three components: a virtual mass term, an advection damping term, and a drag term. The virtual mass and drag terms have been proposed before (Simpson et al., 1965; de Roode et al., 2012; Siebesma et al., 2007; Tan et al., 2018; Han & Bretherton, 2019; Davies-Jones, 2003; Doswell III & Markowski, 2004; Jeevanjee & Romps, 2015); they represent momentum sinks. Additionally, the advection damping term has proven to be an important momentum source at the bottom of convective systems (Schumann & Moeng, 1991; Jeevanjee & Romps, 2015; Morrison, 2016b). Simplified expressions capturing it have been suggested before (Peters, 2016), but they have not been tested in parameterization schemes. LES confirm the perturbation pressure as an important momentum source for thermal bubbles as well as in shallow and deep moist convection. The advection damping term is important for the dynamics of transient convective bubbles, but less so in terms of bulk average properties. This indicates that inclusion of the advection term may be important for simulating transient processes. The drag term is consistent with previous LES diagnostics (Romps & Charn, 2015). Thuburn et al. (2019) and Weller and McIntyre (2019) have additionally shown that it is essential for numerical stability of EDMF-like schemes. The key modification in our drag formula relative to other parameterizations is to replace the horizontal scale by the vertical scale of the updraft. This enables an improved representation of the diurnal cycle of deep convection.

An interesting distinction between a rising bubble and a coherent plume is that the bubble gets detached from the surface at some point in time. As the discontinuous bottom of the bubble rises, the perturbation pressure plays a key role as a momentum source at the bottom. By contrast, a plume remains continuous from the surface upward and does not have a strong momentum source from the perturbation pressure. Mass-flux models for clouds and convection are normally designed based on assuming plumes and have difficulties simulating a rising bubble. The time-dependent parameterization scheme circumvents the distinction between plumes and bubbles (Yano, 2014) and can capture both (Weller et al., 2020).

The extended EDMF scheme has the potential to unify SGS parameterizations of turbulence and convection, given proper closures. The pressure closure presented in this paper, the entrainment and detrainment closures presented in Cohen et al. (2020), and the mixing length closure presented in Lopez-Gomez et al. (2020), allow this parameterization to represent a wide spectrum of different atmospheric boundary layers and convective motions.

Appendix A Pressure Work for Environmental TKE

As assumed in Tan et al. (2018) and Lopez-Gomez et al. (2020), pressure does not do work on the grid-mean TKE, but rather redistributes TKE between the subdomains, that is,

$$-\left\langle \rho u^* \left(\frac{\partial P^\dagger}{\partial x}\right)^* + \rho v^* \left(\frac{\partial P^\dagger}{\partial y}\right)^* + \rho w^* \left(\frac{\partial P^\dagger}{\partial z}\right)^* \right\rangle = 0. \tag{A1}$$

Following (22) and neglecting covariance terms $\overline{\phi_i'\psi_i'}$ except in the environment (i.e., $i = 0$), the grid-mean flux is decomposed into the ED and MF components

$$-\rho a_0 \left[\overline{w_0' \left(\frac{\partial P^\dagger}{\partial z}\right)_0'} + \overline{u_0' \left(\frac{\partial P^\dagger}{\partial x}\right)_0'} + \overline{v_0' \left(\frac{\partial P^\dagger}{\partial y}\right)_0'} \right] - \sum_{i:i\geq 0} \rho a_i \bar{w}_i^* \overline{\left(\frac{\partial P^\dagger}{\partial z}\right)_i}^* = 0. \tag{A2}$$

Separating the environmental and plume contributions from the second term, moving them to the right-hand side and using the relationship $\sum_{i:i\geq 0} a_i \bar{\phi}_i^* = 0$ leads to

$$
\begin{aligned}
-\rho a_0 & \left[\overline{w_0' \left(\frac{\partial P^\dagger}{\partial z}\right)_0'} + \overline{u_0' \left(\frac{\partial P^\dagger}{\partial x}\right)_0'} + \overline{v_0' \left(\frac{\partial P^\dagger}{\partial y}\right)_0'}\right] \\
&= \rho a_0 \bar{w}_0^* \overline{\left(\frac{\partial P^\dagger}{\partial z}\right)_0}^* + \sum_{i:i\geq 1} \rho a_i \bar{w}_i^* \overline{\left(\frac{\partial P^\dagger}{\partial z}\right)_i}^* \\
&= -\rho \bar{w}_0^* \sum_{i:i\geq 1} a_i \overline{\left(\frac{\partial P^\dagger}{\partial z}\right)_i}^* + \sum_{i:i\geq 1} \rho a_i \bar{w}_i^* \overline{\left(\frac{\partial P^\dagger}{\partial z}\right)_i}^* \\
&= \sum_{i:i\geq 1} \rho a_i \left(\bar{w}_i^* - \bar{w}_0^*\right) \overline{\left(\frac{\partial P^\dagger}{\partial z}\right)_i}^*. \qquad \text{(A3)}
\end{aligned}
$$

Appendix B Single-Normal Mode Solution for Axisymmetric Thermals

In the axisymmetric cylindrical coordinate system, the mass continuity equation is

$$\frac{\partial (ur)}{\partial r} + \frac{\partial (wr)}{\partial z} = 0, \qquad \text{(B1)}$$

where r and u denote the radial direction originating from the thermal's central axis and the radial velocity, z and w denote the vertical direction and vertical velocity.

The pressure Poisson equation in the axisymmetric cylindrical coordinate system is

$$\nabla^2_{r,z} P^\dagger = \frac{\partial b}{\partial z} - \left[\left(\frac{\partial u}{\partial r}\right)^2 + \left(\frac{u}{r}\right)^2 + \left(\frac{\partial w}{\partial z}\right)^2\right] - 2\frac{\partial u}{\partial z}\frac{\partial w}{\partial r}. \qquad \text{(B2)}$$

Using the mass continuity equation, it simplifies to

$$\nabla^2_{r,z} P^\dagger = \frac{\partial b}{\partial z} - 2\left[\left(\frac{\partial w}{\partial z}\right)^2 + \frac{\partial u}{\partial z}\frac{\partial w}{\partial r} - \frac{u}{r}\frac{\partial u}{\partial r}\right], \qquad \text{(B3)}$$

where

$$\nabla^2_{r,z} = \frac{1}{r}\frac{\partial}{\partial r} r \frac{\partial}{\partial r} + \frac{\partial^2}{\partial z^2}.$$

The perturbation pressure potential is decomposed into the sum of buoyancy and dynamic perturbation pressure, i.e., $P^\dagger = P_\mathrm{b} + P_\mathrm{d}$ such that

$$
\begin{aligned}
\nabla^2_{r,z} P_\mathrm{b} &= \frac{\partial b}{\partial z}, \\
\nabla^2_{r,z} P_\mathrm{d} &= -2\left[\left(\frac{\partial w}{\partial z}\right)^2 + \frac{\partial u}{\partial z}\frac{\partial w}{\partial r} - \frac{u}{r}\frac{\partial u}{\partial r}\right].
\end{aligned} \qquad \text{(B4)}
$$

For an axisymmetric thermal bubble, a trigonometric basis is used for the vertical wave structure, as for the 2D derivation, while Bessel functions of the first kind $J_\alpha(\cdot)$ are used for the horizontal structure, to exploit eigenfunctions of the Laplacian operator (Holton, 1973). That is

$$
\begin{aligned}
b &= b_A \sin(mz) J_0(k_b r), \\
w &= w_A \sin(mz) J_0(k_w r), \\
u &= u_A \cos(mz) J_1(k_w r),
\end{aligned} \qquad \text{(B5)}
$$

where $m = \pi H^{-1}$ is the vertical wavenumber, and $k_b = 2.4R^{-1}$ ensures k_bR is the first zero of the Bessel function, $J_0(k_bR) = 0$. The parameter R is the boundary for the thermal where buoyancy switches sign. Meanwhile, the flow satisfies a free-slip boundary condition at the thermal edges (where $J_1(k_wR) = 0$), which gives $k_w = 3.83R^{-1}$. Then, combining (B1) and (B5), with the identities of Bessel functions ($\frac{d}{dx}[xJ_1(x)] = xJ_0(x)$ and $\frac{d}{dx}J_0(x) = -J_1(x)$), gives

$$k_w u_A + m w_A = 0, \tag{B6}$$

which is essential for simplifying the following derivation. The buoyancy and velocity structures of the axisymmetric thermal are shown in the bottom row of Figure 1.

B1 Buoyancy Perturbation Pressure

The buoyancy perturbation pressure satisfies

$$\nabla^2_{r,z} P_\mathrm{b} = m b_A \cos{(mz)} J_0(k_b r). \tag{B7}$$

With the eigenfunction ansatz, this can be solved to give

$$P_\mathrm{b} = -\frac{m}{m^2 + k_b^2} b_A \cos{(mz)} J_0(k_b r), \tag{B8}$$

which gives the buoyancy perturbation pressure gradient as

$$\frac{\partial P_\mathrm{b}}{\partial z} = \frac{m^2}{m^2 + k_b^2} b_A \sin{(mz)} J_0(k_b r) = \frac{1}{1 + (\frac{4.8}{\pi}\frac{H}{2R})^2} b. \tag{B9}$$

The buoyancy perturbation pressure gradient for a 3D thermal is

$$\left[1 + \left(\frac{4.8}{\pi}\frac{H}{2R}\right)^2\right]^{-1} b, \tag{B10}$$

which reaches the same formulation as the single-normal mode solution derived in Morrison (2016b).

Similar to the 2D thermal, applying the conditional average over all the 3D thermals within the i-th subdomain yields

$$-\overline{\left(\frac{\partial P_\mathrm{b}}{\partial z}\right)_i}^* = \sum_{j=1}^{N} -\frac{1}{1 + \left(\frac{4.8}{\pi}\frac{H_j}{2R_j}\right)^2} \eta \bar{b}_i^* = -\eta \arctan\left(\frac{4.8}{\pi}\frac{H}{2R}\right) \bar{b}_i^*. \tag{B11}$$

B2 Dynamic Perturbation Pressure

In cylindrical coordinates, the dynamic pressure includes a third term arising from the curvature of the coordinate system. The expansion of the dynamic perturbation pressure is done separately for each of the three terms, as follows:

$$\begin{aligned}\left(\frac{\partial w}{\partial z}\right)^2 =& \left(m w_A \cos{(mz)} J_0(k_w r)\right)^2 \\ =& \frac{m^2}{2} w_A^2 \left(1 + \cos{(2mz)}\right) J_0^2(k_w r),\end{aligned} \tag{B12}$$

$$\begin{aligned}\frac{\partial u}{\partial z}\frac{\partial w}{\partial r} =& \left[-m u_A \sin{(mz)} J_1(k_w r)\right]\left[w_A \sin{(mz)} \left(-k_w J_1(k_w r)\right)\right] \\ =& m k_w u_A w_A \sin^2 mz J_1^2(k_w r) \\ =& -\frac{m^2}{2} w_A^2 \left(1 - \cos{(2mz)}\right) J_1^2(k_w r),\end{aligned} \tag{B13}$$

$$
\begin{aligned}
-\frac{u}{r}\frac{\partial u}{\partial r} =& -\left[\frac{u_A}{r}\cos(mz)J_1(k_w r)\right]\left[u_A\cos(mz)\left(k_w J_0(k_w r) - \frac{J_1(k_w r)}{r}\right)\right] \\
=& -\frac{u_A^2}{2}\left(1+\cos(2mz)\right)\left(\frac{k_w J_0(k_w r)J_1(k_w r)}{r} - \frac{J_1^2(k_w r)}{r^2}\right).
\end{aligned}
\tag{B14}
$$

Using these expansions, the Poisson equation for dynamic perturbation pressure can be written as

$$
\begin{aligned}
\nabla_{r,z}^2 P_\mathrm{d} =& -2\left[\left(\frac{\partial w}{\partial z}\right)^2 + \frac{\partial u}{\partial z}\frac{\partial w}{\partial r} - \frac{u}{r}\frac{\partial u}{\partial r}\right] \\
=& -m^2 w_A^2\left(1+\cos(2mz)\right)J_0^2(k_w r) + m^2 w_A^2\left(1-\cos(2mz)\right)J_1^2(k_w r) \\
&+ u_A^2\left(1+\cos(2mz)\right)\left(\frac{k_w J_0(k_w r)J_1(k_w r)}{r} - \frac{J_1^2(k_w r)}{r^2}\right) \\
=& -m^2 w_A^2 J_0^2(k_w r) - m^2 w_A^2\cos(2mz)J_0^2(k_w r) + m^2 w_A^2 J_1^2(k_w r) - m^2 w_A^2\cos(2mz)J_1^2(k_w r) \\
&+ m^2 w_A^2\left(1+\cos(2mz)\right)\left[\frac{J_0(k_w r)J_1(k_w r)}{k_w r} - \frac{J_1^2(k_w r)}{k_w^2 r^2}\right].
\end{aligned}
\tag{B15}
$$

Dividing both sides by $m^2 w_A^2$ and re-organizing the right-hand-side terms simplifies (B15) into

$$
\begin{aligned}
\nabla_{r,z}^2\frac{P_\mathrm{d}}{m^2 w_A^2} =& \underbrace{\left(-J_0^2(k_w r) + J_1^2(k_w r) + \underbrace{\left[\frac{J_0(k_w r)J_1(k_w r)}{k_w r} - \frac{J_1^2(k_w r)}{k_w^2 r^2}\right]}_{A'}\right)}_{A} \\
&+ \underbrace{\cos(2mz)\left(-J_0^2(k_w r) - J_1^2(k_w r) + \left[\frac{J_0(k_w r)J_1(k_w r)}{k_w r} - \frac{J_1^2(k_w r)}{k_w^2 r^2}\right]\right)}_{B}.
\end{aligned}
\tag{B16}
$$

Term A' comes from $\frac{1}{x}\frac{d}{dx}x\frac{d}{dx}J_1^2$. Similarly, $\frac{1}{x}\frac{d}{dx}x\frac{d}{dx}$ operating on J_0^2 and J_1^2 also gives J_0^2 and J_1^2 terms. However, J_0^2 and J_1^2 are not orthogonal functions. With the orthogonality properties of Bessel functions of the same order, we will perform a Fourier-Bessel series expansion using the zeroth order Bessel functions as basis.

We expand term A in (B16) into Fourier-Bessel series as

$$
g(x) = -J_0^2(x) + J_1^2(x) + \left[\frac{J_0(x)J_1(x)}{x} - \frac{J_1^2(x)}{x^2}\right] = \sum_{n=1}^{\infty} c_{n,g}J_0\left(\frac{u_{0,n}}{b}x\right),
\tag{B17}
$$

where $x = k_w r$ and $b \approx 4.6317$ gives $g(b) = 0$; $u_{0,n}$ is the n-th root for $J_0(x) = 0$, and $c_{n,g}$ is the expansion coefficients calculated as

$$
c_{n,g} = \frac{\int_0^b x g(x) J_0(u_{0,n}x/b)dx}{0.5[bJ_1(u_{0,n})]^2}.
\tag{B18}
$$

We then write term B in (B16) as

$$
h(x) = -J_0^2(x) - J_1^2(x) + \left[\frac{J_0(x)J_1(x)}{x} - \frac{J_1^2(x)}{x^2}\right],
\tag{B19}
$$

and let

$$
\tilde{h}(x) = h(x) - h(b),
\tag{B20}
$$

so that $\tilde{h}(b) = 0$, and we can expand $\tilde{h}(x)$ into Fourier-Bessel series in the same interval $[0, b]$ as for $g(x)$. The transformation in (B20) makes sure terms A and B are expanded to orthogonal basis in the same interval, that is

$$h(x) = h(b) + \tilde{h}(x) = h(b) + \sum_{n=1}^{\infty} c_{n,h} J_0\left(\frac{u_{0,n}}{b}x\right), \tag{B21}$$

where $x = k_w r$, b, and $u_{0,n}$ are the same as in the $g(x)$ expansion, and $c_{n,f}$ is the coefficient for the Fourier-Bessel expansion for $\tilde{h}$,

$$c_{n,h} = \frac{\int_0^b x\tilde{h}(x) J_0(u_{0,n}x/b)dx}{0.5[bJ_1(u_{0,n})]^2}. \tag{B22}$$

Substituting A and B in (B16) by (B17) and (B21), the Fourier-Bessel expansion of the Poisson equation becomes

$$\begin{aligned}\nabla^2_{r,z}\frac{P_\mathrm{d}}{m^2 w_A^2} =& g(k_w r) + \cos(2mz) h(k_w r) \\ =& \sum_{n=1}^{\infty} c_{n,g} J_0\left(\frac{u_{0,n}}{b}k_w r\right) + \cos(2mz)\left[h(b) + \sum_{n=1}^{\infty} c_{n,h} J_0\left(\frac{u_{0,n}}{b}k_w r\right)\right].\end{aligned} \tag{B23}$$

Similar to the 2D derivation, we use an ansatz for $P_\mathrm{d}/(m^2 w_A^2)$ of

$$\frac{P_d}{m^2 w_A^2} = \sum_{m=1}^{\infty} G_n J_0\left(\frac{u_{0,n}}{b}k_w r\right) + \cos(2mz)\sum_{m=1}^{\infty} H_n J_0\left(\frac{u_{0,n}}{b}k_w r\right) + X\cos(2mz) + Fz, \tag{B24}$$

where G_n, H_n, and X need to be solved for by combining (B24) and (B23); F corresponds to the drag coefficient and is obtained in the same way as the 2D case.

Taking the Laplacian of (B24) gives

$$\begin{aligned}\nabla^2_{r,z}\frac{P_d}{m^2 w_A^2} =& \sum_{n=1}^{\infty} G_n\left[-\frac{u_{0,n}^2}{b^2}k_w^2\right] J_0\left(\frac{u_{0,n}}{b}k_w r\right) + \cos(2mz)\left(\sum_{n=1}^{\infty} H_n\left[-\frac{u_{0,n}^2}{b^2}k_w^2\right] J_0\left(\frac{u_{0,n}}{b}k_w r\right)\right) \\ & - 4m^2\cos(2mz)\sum_{m=1}^{\infty} H_n J_0\left(\frac{u_{0,n}}{b}k_w r\right) - 4m^2 X\cos(2mz).\end{aligned} \tag{B25}$$

With the orthogonality between $J_0(\frac{u_{0,n}}{b}kr)$ and $J_0(\frac{u_{0,m}}{b}kr)$ $m \neq n$, the coefficients are obtained from

$$\begin{aligned} -\frac{u_{0,n}^2}{b^2}k_w^2 G_n =& c_{n,g}, \\ -\frac{u_{0,n}^2}{b^2}k_w^2 H_n - 4m^2 H_n =& c_{n,h}, \\ -4m^2 X =& h(b),\end{aligned} \tag{B26}$$

as

$$\begin{aligned} G_n =& -\frac{b^2 c_{n,g}}{u_{0,n}^2 k_w^2}, \\ H_n =& -\frac{b^2 c_{n,h}}{u_{0,n}^2 k_w^2 + 4m^2 b^2}, \\ X =& -\frac{h(b)}{4m^2},\end{aligned} \tag{B27}$$

where $c_{n,g}$ and $c_{n,h}$ are obtained from the orthogonality of J_0 as in (B18) and (B22), and $h(b) \approx -0.1394$.

The drag term F is obtained in the same way as the 2D case. We have

$$\int_0^{2\pi} d\theta \int_0^R \rho[P_\mathrm{d} + \frac{1}{2}w^2]_{z=0}^{z=H} rdr = \frac{1}{2}\rho A c_d w_r^2 \tag{B28}$$

where $A = \pi R^2$, and it solves

$$F = \frac{1}{2}c_d \frac{w_r^2}{H}. \tag{B29}$$

We obtain the vertical gradient of dynamic perturbation pressure as

$$\begin{aligned} -\frac{\partial P_d}{\partial z} =& 2m^3 w_A^2 \sin{(2mz)} \sum_{m=1}^{\infty} H_n J_0(\frac{u_{0,n}}{b}kr) - \frac{h(b)}{2} m w_A^2 \sin{(2mz)} - F \\ =& 4m^2 w_A \sin{(mz)} \frac{d}{dz}[w_A \sin{(mz)}] \sum_{m=1}^{\infty} H_n J_0(\frac{u_{0,n}}{b}k_w r) - h(b) w_A \sin{(mz)} \frac{d}{dz}[w_A \sin{(mz)}] - F. \end{aligned} \tag{B30}$$

To implement the perturbation pressure in the EDMF scheme, we perform a conditional average by applying

$$\sum_{j=1}^{N} \frac{1}{\pi R_j^2} \int_0^{2\pi} d\theta \int_0^{R_j} (\cdot) rdr$$

on (B30):

$$-\overline{\left(\frac{\partial P_d}{\partial z}\right)}_i = \Gamma(m, k_w)\overline{w}_i \frac{d\overline{w}_i}{dz} - \alpha_d \frac{(\overline{w}_i - \overline{w}_0)|\overline{w}_i - \overline{w}_0|}{H_i}. \tag{B31}$$

Here, the coefficient for the advective term,

$$\Gamma(k, m) = \sum_{j=1}^{N} \frac{1}{\pi R_j^2} \int_0^{2\pi} d\theta \int_0^{R_j} \left(4\gamma^2 m_j^2 \sum_{m=1}^{\infty} H_n J_0\left(\frac{u_{0,n}}{b} k_{w,j} r\right)\right) rdr - h(b),$$

has a complicated dependence on k and m and the Fourier-Bessel series coefficients H_n from (B27).

The 3D analytical solution (B11) and (B31) demonstrates the same combination of physical contributions to the perturbation pressure gradient force for the vertical momentum as the 2D solution. The parameters used in the scheme differ between 2D and 3D and are best learned empirically from data.

Appendix C A Multi-mode Representation for Thermals

The single-normal mode approximation aims to describe the pressure field inside a thermal. In atmospheric flow, convection is driven by a multitude of short-lived successive thermals that are represented in aggregate as towering updraft systems (e.g., Moser and Lasher-Trapp (2017), Morrison et al. (2020)).

In the single-normal mode framework, the spatial structure of an aggregate of thermal bubbles of different horizontal scales R_i and vertical scales H_i, centered at the centroid of the thermal, is

$$\begin{aligned} b &= \sum_{i=1}^{N} b_{A,i} \cos{(m_i z)} \cos{(k_{b,i} x)} h_b(R_i, H_i), \\ w &= \sum_{i=1}^{N} w_{A,i} \cos{(m_i z)} \cos{(k_{w,i} x)} h_b(R_i, H_i). \end{aligned} \tag{C1}$$

Here, h_b is defined as the product of Heaviside functions $h(\cdot)$

$$h_b(R_i, H_i) = h(R_i^2 - x^2) h(H_i^2 - 4z^2), \tag{C2}$$

and $(x = 0, z = 0)$ is the centroid of the thermal. Note that this frame of reference is different from the one used in (6) to facilitate the composite analysis of multi-thermals with respect to their centroids. Also note that h_b is zero outside the thermal bubble. This yields the buoyancy perturbation pressure

$$P_\mathrm{b} = \sum_{i=1}^{N} \frac{m_i}{m_i^2 + k_{b,i}^2} b_{A,i} \sin(m_i z) \cos(k_{b,i} x) h_b(R_i, H_i), \tag{C3}$$

and the dynamic perturbation pressure

$$P_\mathrm{d} = \sum_{i=1}^{N} \Big[-\frac{w_{A,i}^2}{4} \cos(2m_i z) + \frac{m_i^2 w_{A,i}^2}{4k_{w,i}^2} \cos(2k_{w,i} x) \Big] h_b(R_i, H_i) + Fz. \tag{C4}$$

Thus, the vertical gradients are

$$\begin{aligned} -\frac{\partial P_\mathrm{b}}{\partial z} &= -\sum_{i=1}^{N} \frac{m_i^2}{m_i^2 + k_{b,i}^2} b_{A,i} \cos(m_i z) \cos(k_{b,i} x) h_b(R_i, H_i), \\ -\frac{\partial P_\mathrm{d}}{\partial z} &= \sum_{i=1}^{N} w_{A,i} \cos(m_i z) \frac{d}{dz} [w_{A,i} \cos(m_i z)] h_b(R_i, H_i) - c_d \frac{w_r^2}{H}. \end{aligned} \tag{C5}$$

In (C5), w_r and H represent the relative vertical velocity and height of the whole ensemble, respectively. Figure C1 sketches the buoyancy, velocity, and perturbation pressure patterns for an ensemble of 4 thermals with varying R_i but with the same $H_i = H$. The perturbation pressure structure here is consistent with the patterns shown in the idealized simulations in Morrison (2016b).

Acknowledgments

This research was made possible by the generosity of Eric and Wendy Schmidt by recommendation of the Schmidt Futures program, by the Paul G. Allen Family Foundation, and the National Science Foundation (NSF, award AGS-1835860). We would like to thank the Resnick Sustainability Institute at Caltech for fellowship support. Parts of the research were carried out at the Jet Propulsion Laboratory, California Institute of Technology, under a contract with the National Aeronautics and Space Administration and funded through the internal Research and Technology Development program. The PyCLES code used to generate LES results is available at `climate-dynamics.org/software/#pycles`. The SCM code is available at `https://doi.org/10.5281/zenodo.4291143`.

References

Bony, S., & Dufresne, J.-L. (2005). Marine boundary layer clouds at the heart of tropical cloud feedback uncertainties in climate models. *Geophysical Research Letters*, *32*(20). doi: https://doi.org/10.1029/2005GL023851

Bony, S., Stevens, B., Frierson, D. M., Jakob, C., Kageyama, M., Pincus, R., ... others (2015). Clouds, circulation and climate sensitivity. *Nature Geoscience*, *8*(4), 261–268. doi: 0.1038/ngeo2398

Bretherton, C. S., & Park, S. (2009). A new moist turbulence parameterization in the community atmosphere model. *Journal of Climate*, *22*(12), 3422–3448. doi: https://doi.org/10.1175/2008JCLI2556.1

Brient, F., & Schneider, T. (2016). Constraints on climate sensitivity from space-based measurements of low-cloud reflection. *Journal of Climate*, *29*(16), 5821–5835. doi: https://doi.org/10.1175/JCLI-D-15-0897.1

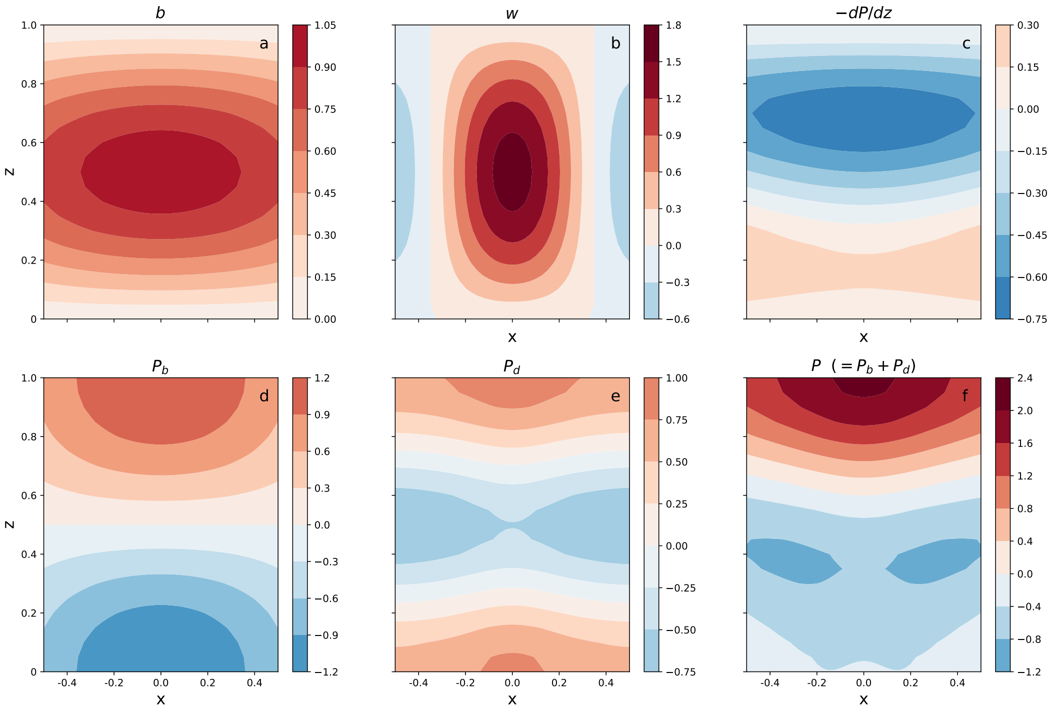

Figure C1. The structures for buoyancy (a), vertical velocity (b), vertical pressure gradient force (c), P_b (d), P_d (e), and perturbation pressure ($P_\mathrm{b} + P_\mathrm{d}$) (f) for an ensemble of 4 thermals. The thermal is created by specifying dimensionless $H = 1$ and varying horizontal scale $[0.2, 0.333, 0.467, 0.6]$.

Bryan, G. H., & Fritsch, J. M. (2002). A benchmark simulation for moist nonhydrostatic numerical models. *Monthly Weather Review*, *130*(12), 2917–2928. doi: https://doi.org/10.1175/1520-0493(2002)130⟨2917:ABSFMN⟩2.0.CO;2

Caldwell, P. M., Zelinka, M. D., & Klein, S. A. (2018). Evaluating emergent constraints on equilibrium climate sensitivity. *Journal of Climate*, *31*(10), 3921–3942. doi: 10.1175/JCLI-D-17-0631.1

Ceppi, P., Brient, F., Zelinka, M. D., & Hartmann, D. L. (2017). Cloud feedback mechanisms and their representation in global climate models. *Wiley Interdisciplinary Reviews: Climate Change*, *8*(4), e465. doi: 10.1002/wcc.465

Cleary, E., Garbuno-Inigo, A., Lan, S., Schneider, T., & Stuart, A. M. (2021). Calibrate, emulate, sample. *J. Comp. Phys.*, *424*, 109716.

Cohen, Y., Lopez-Gomez, I., Jaruga, A., He, J., Kaul, C. M., & Schneider, T. (2020). Unified entrainment and detrainment closures for extended eddy-diffusivity mass-flux schemes. *Journal of Advances in Modeling Earth Systems*, *12*(9), e2020MS002162. doi: 10.1029/2020MS002162

Couvreux, F., Hourdin, F., & Rio, C. (2010). Resolved versus parametrized boundary-layer plumes. part i: A parametrization-oriented conditional sampling in large-eddy simulations. *Boundary-layer meteorology*, *134*(3), 441–458. doi: 10.1007/s10546-009-9456-5

Dai, A., & Trenberth, K. E. (2004). The diurnal cycle and its depiction in the community climate system model. *Journal of Climate*, *17*(5), 930–951. doi: https://doi.org/10.1175/1520-0442(2004)017⟨0930:TDCAID⟩2.0.CO;2

Davies-Jones, R. (2003). An expression for effective buoyancy in surroundings with horizontal density gradients. *Journal of the atmospheric sciences*, *60*(23), 2922–2925. doi: https://doi.org/10.1175/1520-0469(2003)060⟨2922:AEFEBI⟩2.0.CO;2

de Roode, S. R., Siebesma, A. P., Jonker, H. J. J., & de Voogd, Y. (2012). Parameterization of the vertical velocity equation for shallow cumulus clouds. *Monthly Weather Review*, *140*(8), 2424-2436. doi: 10.1175/MWR-D-11-00277.1

Doswell III, C. A., & Markowski, P. M. (2004). Is buoyancy a relative quantity? *Monthly weather review*, *132*(4), 853–863. doi: https://doi.org/10.1175/1520-0493(2004)132⟨0853:IBARQ⟩2.0.CO;2

Giordani, H., Bourdallé-Badie, R., & Madec, G. (2020). An eddy-diffusivity mass-flux parameterization for modelling oceanic convection. *Journal of Advances in Modeling Earth Systems*, e2020MS002078. doi: https://doi.org/10.1029/2020MS002078

Golaz, J.-C., Larson, V. E., & Cotton, W. R. (2002a). A pdf-based model for boundary layer clouds. part ii: Model results. *Journal of the Atmospheric Sciences*, *59*(24), 3552-3571. doi: https://doi.org/10.1175/1520-0469(2002)059⟨3552:APBMFB⟩2.0.CO;2

Golaz, J.-C., Larson, V. E., & Cotton, W. R. (2002b). A pdf-based model for boundary layer clouds. part i: Method and model description. *Journal of the Atmospheric Sciences*, *59*(24), 3540-3551. doi: https://doi.org/10.1175/1520-0469(2002)059⟨3540:APBMFB⟩2.0.CO;2

Grabowski, W., Bechtold, P., Cheng, A., Forbes, R., Halliwell, C., Khairoutdinov, M., … et al. (2006). Daytime convective development over land: A model intercomparison based on lba observations. *Quarterly Journal of the Royal Meteorological Society*, *132*(615), 317–344. doi: doi.org/10.1256/qj.04.147

Gu, J.-F., Plant, R. S., Holloway, C. E., Jones, T. R., Stirling, A., Clark, P. A., … Webb, T. L. (2020). Evaluation of the bulk mass flux formulation using large-eddy simulations. *Journal of the Atmospheric Sciences*, *77*(6), 2115–2137. doi: https://doi.org/10.1175/JAS-D-19-0224.1

Han, J., & Bretherton, C. S. (2019). Tke-based moist eddy-diffusivity mass-flux (edmf) parameterization for vertical turbulent mixing. *Weather and Forecasting*, *34*(4), 869-886. doi: 10.1175/WAF-D-18-0146.1

Heinze, R., Mironov, D., & Raasch, S. (2015). Second-moment budgets in cloud topped boundary layers: A large-eddy simulation study. *Journal of Advances in Modeling Earth Systems*, *7*(2), 510-536. doi: 10.1002/2014MS000376

Hernandez-Deckers, D., & Sherwood, S. C. (2016). A numerical investigation of cumulus thermals. *Journal of the Atmospheric Sciences*, *73*(10), 4117–4136.

Holland, J. Z., & Rasmusson, E. M. (1973). Measurements of the atmospheric mass, energy, and momentum budgets over a 500-kilometer square of tropical ocean. *Monthly Weather Review*, *101*(1), 44–57. doi: 10.1175/1520-0493(1973)101⟨0044:MOTAME⟩2.3.CO;2

Holton, J. R. (1973). A one-dimensional cumulus model including pressure perturbations. *Monthly Weather Review*, *101*(3), 201-205. doi: 10.1175/1520-0493(1973)101⟨0201:AOCMIP⟩2.3.CO;2

Holtslag, A., Svensson, G., Baas, P., Basu, S., Beare, B., Beljaars, A., . . . others (2013). Stable atmospheric boundary layers and diurnal cycles: challenges for weather and climate models. *Bulletin of the American Meteorological Society*, *94*(11), 1691–1706. doi: https://doi.org/10.1175/BAMS-D-11-00187.1

Jeevanjee, N., & Romps, D. M. (2015). Effective buoyancy, inertial pressure, and the mechanical generation of boundary layer mass flux by cold pools. *Journal of the Atmospheric Sciences*, *72*(8), 3199-3213. doi: 10.1175/JAS-D-14-0349.1

Jeevanjee, N., & Romps, D. M. (2016). Effective buoyancy at the surface and aloft. *Quarterly Journal of the Royal Meteorological Society*, *142*(695), 811–820. doi: https://doi.org/10.1002/qj.2683

Lappen, C.-L., & Randall, D. A. (2001a). Toward a unified parameterization of the boundary layer and moist convection. part i: A new type of mass-flux model. *Journal of the Atmospheric Sciences*, *58*(15), 2021-2036. doi: https://doi.org/10.1175/1520-0469(2001)058⟨2021:TAUPOT⟩2.0.CO;2

Lappen, C.-L., & Randall, D. A. (2001b). Toward a unified parameterization of the boundary layer and moist convection. part iii: Simulations of clear and cloudy convection. *Journal of the Atmospheric Sciences*, *58*(15), 2052-2072. doi: https://doi.org/10.1175/1520-0469(2001)058⟨2052:TAUPOT⟩2.0.CO;2

Lappen, C.-L., & Randall, D. A. (2001c). Toward a unified parameterization of the boundary layer and moist convection. part ii: Lateral mass exchanges and subplume-scale fluxes. *Journal of the Atmospheric Sciences*, *58*(15), 2037-2051. doi: https://doi.org/10.1175/1520-0469(2001)058⟨2037:TAUPOT⟩2.0.CO;2

Lappen, C.-L., & Randall, D. A. (2006). Parameterization of pressure perturbations in a pbl mass-flux model. *Journal of the atmospheric sciences*, *63*(7), 1726–1751. doi: https://doi.org/10.1175/JAS3722.1

Larson, V. E., & Golaz, J.-C. (2005). Using probability density functions to derive consistent closure relationships among higher-order moments. *Monthly Weather Review*, *133*(4), 1023–1042. doi: 10.1175/MWR2902.1

Leger, J., Lafore, J.-P., Piriou, J.-M., & Guérémy, J.-F. (2019). A simple model of convective drafts accounting for the perturbation pressure term. *Journal of the Atmospheric Sciences*, *76*(10), 3129-3149. doi: 10.1175/JAS-D-18-0281.1

Levine, J. (1959). Spherical vortex theory of bubble-like motion in cumulus clouds. *Journal of Atmospheric Sciences*, *16*(6), 653–662.

Liu, L., Zhu, J., & Wu, J. (2015). Lift and drag in two-dimensional steady viscous and compressible flow. *Journal of Fluid Mechanics*, *784*, 304.

Lopez-Gomez, I., Cohen, Y., He, J., Jaruga, A., & Schneider, T. (2020). A generalized mixing length closure for eddy-diffusivity mass-flux schemes of turbulence and convection. *Journal of Advances in Modeling Earth Systems*, e2020MS002161. doi: 10.1029/2020MS002161

Morrison, H. (2016a). Impacts of updraft size and dimensionality on the perturbation pressure and vertical velocity in cumulus convection. part ii: Comparison of theoretical and numerical solutions and fully dynamical simulations. *Journal of the Atmospheric Sciences*, *73*(4), 1455–1480.

Morrison, H. (2016b). Impacts of updraft size and dimensionality on the perturbation pressure and vertical velocity in cumulus convection. part i: Simple, generalized analytic solutions. *Journal of the Atmospheric Sciences*, *73*(4), 1441-1454. doi: 10.1175/JAS-D-15-0040.1

Morrison, H., & Peters, J. M. (2018). Theoretical expressions for the ascent rate of moist deep convective thermals. *Journal of the Atmospheric Sciences*, *75*(5), 1699–1719.

Morrison, H., Peters, J. M., & Sherwood, S. C. (2021). Comparing growth rates of simulated moist and dry convective thermals. *Journal of the Atmospheric Sciences*, *78*(3), 797–816.

Morrison, H., Peters, J. M., Varble, A. C., Hannah, W. M., & Giangrande, S. E. (2020). Thermal chains and entrainment in cumulus updrafts. part i: Theoretical description. *Journal of the Atmospheric Sciences*, *77*(11), 3637–3660.

Moser, D. H., & Lasher-Trapp, S. (2017). The influence of successive thermals on entrainment and dilution in a simulated cumulus congestus. *Journal of the Atmospheric Sciences*, *74*(2), 375–392.

Murphy, J. M., Sexton, D. M., Barnett, D. N., Jones, G. S., Webb, M. J., Collins, M., & Stainforth, D. A. (2004). Quantification of modelling uncertainties in a large ensemble of climate change simulations. *Nature*, *430*(7001), 768–772. doi: 10.1038/nature02771

Park, S. (2014a). A unified convection scheme (unicon). part i: Formulation. *Journal of the Atmospheric Sciences*, *71*(11), 3902–3930. doi: https://doi.org/10.1175/JAS-D-13-0233.1

Park, S. (2014b). A unified convection scheme (unicon). part ii: Simulation. *Journal of the Atmospheric Sciences*, *71*(11), 3931–3973. doi: https://doi.org/10.1175/JAS-D-13-0234.1

Peters, J. M. (2016). The impact of effective buoyancy and dynamic pressure forcing on vertical velocities within two-dimensional updrafts. *Journal of the Atmospheric Sciences*, *73*(11), 4531-4551. doi: 10.1175/JAS-D-16-0016.1

Peters, J. M., Morrison, H., Varble, A. C., Hannah, W. M., & Giangrande, S. E. (2020). Thermal chains and entrainment in cumulus updrafts. part ii: Analysis of idealized simulations. *Journal of Atmospheric Sciences*, *77*(11), 3661–3681.

Pressel, K. G., Kaul, C. M., Schneider, T., Tan, Z., & Mishra, S. (2015). Large-eddy simulation in an anelastic framework with closed water and entropy balances. *Journal of Advances in Modeling Earth Systems*, *7*(3), 1425–1456. doi: https://doi.org/10.1002/2015MS000496

Romps, D. M., & Charn, A. B. (2015). Sticky thermals: Evidence for a dominant balance between buoyancy and drag in cloud updrafts. *Journal of the Atmospheric Sciences*, *72*(8), 2890-2901. doi: 10.1175/JAS-D-15-0042.1

Sánchez, O., Raymond, D. J., Libersky, L., & Petschek, A. G. (1989). The development of thermals from rest. *Journal of the atmospheric sciences*, *46*(14), 2280–2292. doi: https://doi.org/10.1175/1520-0469(1989)046⟨2280:TDOTFR⟩2.0.CO;2

Schneider, T., Teixeira, J., Bretherton, C. S., Brient, F., Pressel, K. G., Schär, C., & Siebesma, A. P. (2017). Climate goals and computing the future of clouds. *Nature Climate Change*, *7*(1), 3–5. doi: https://doi.org/10.1038/nclimate3190

Schumann, U., & Moeng, C.-H. (1991). Plume budgets in clear and cloudy convective boundary layers. *Journal of the Atmospheric Sciences*, *48*(15), 1758-1770. doi: 10.1175/1520-0469(1991)048⟨1758:PBICAC⟩2.0.CO;2

Shen, Z., Pressel, K. G., Tan, Z., & Schneider, T. (2020). Statistically steady state large-eddy simulations forced by an idealized gcm: 1. forcing framework and simulation characteristics. *Journal of Advances in Modeling Earth Systems*, *12*(2), e2019MS001814.

Sherwood, S. C., Hernández-Deckers, D., Colin, M., & Robinson, F. (2013). Slippery thermals and the cumulus entrainment paradox. *Journal of the Atmospheric*

Sciences, *70*(8), 2426–2442.
Siebesma, A. P., Bretherton, C. S., Brown, A., Chlond, A., Cuxart, J., Duynkerke, P. G., … others (2003). A large eddy simulation intercomparison study of shallow cumulus convection. *Journal of the Atmospheric Sciences*, *60*(10), 1201–1219.
Siebesma, A. P., Soares, P. M. M., & Teixeira, J. (2007). A combined eddy-diffusivity mass-flux approach for the convective boundary layer. *Journal of the Atmospheric Sciences*, *64*(4), 1230-1248. doi: 10.1175/JAS3888.1
Simpson, J., Simpson, R. H., Andrews, D. A., & Eaton, M. A. (1965). Experimental cumulus dynamics. *Reviews of Geophysics*, *3*(3), 387-431. doi: 10.1029/RG003i003p00387
Simpson, J., & Wiggert, V. (1969). Models of precipitating cumulus towers. *Mon. Wea. Rev*, *97*(7), 471–489. doi: https://doi.org/10.1175/1520-0493(1969)097⟨0471:MOPCT⟩2.3.CO;2
Soares, P. M. M., Miranda, P. M. A., Siebesma, A. P., & Teixeira, J. (2004). An eddy-diffusivity/mass-flux parametrization for dry and shallow cumulus convection. *Quarterly Journal of the Royal Meteorological Society*, *130*(604), 3365-3383. doi: 10.1256/qj.03.223
Suselj, K., Kurowski, M. J., & Teixeira, J. (2019). On the factors controlling the development of shallow convection in eddy-diffusivity/mass-flux models. *Journal of the Atmospheric Sciences*, *76*(2), 433-456. doi: 10.1175/JAS-D-18-0121.1
Tan, Z., Kaul, C. M., Pressel, K. G., Cohen, Y., Schneider, T., & Teixeira, J. (2018). An extended eddy-diffusivity mass-flux scheme for unified representation of subgrid-scale turbulence and convection. *Journal of Advances in Modeling Earth Systems*, *10*(3), 770-800. doi: 10.1002/2017MS001162
Tarshish, N., Jeevanjee, N., & Lecoanet, D. (2018). Buoyant motion of a turbulent thermal. *Journal of the Atmospheric Sciences*, *75*(9), 3233-3244. doi: 10.1175/JAS-D-17-0371.1
Teixeira, J., Cardoso, S., Bonazzola, M., Cole, J., DelGenio, A., DeMott, C., … others (2011). Tropical and subtropical cloud transitions in weather and climate prediction models: The gcss/wgne pacific cross-section intercomparison (gpci). *Journal of Climate*, *24*(20), 5223–5256. doi: 10.1175/2011JCLI3672.1
Thuburn, J., Efstathiou, G. A., & Beare, R. J. (2019). A two-fluid single-column model of the dry, shear-free, convective boundary layer. *Quarterly Journal of the Royal Meteorological Society*, *145*(721), 1535–1550. doi: 10.1002/qj.3510
Thuburn, J., Weller, H., Vallis, G. K., Beare, R. J., & Whitall, M. (2018). A framework for convection and boundary layer parameterization derived from conditional filtering. *Journal of the Atmospheric Sciences*, *75*(3), 965-981. doi: 10.1175/JAS-D-17-0130.1
Webb, M. J., Lambert, F. H., & Gregory, J. M. (2013). Origins of differences in climate sensitivity, forcing and feedback in climate models. *Climate Dynamics*, *40*(3-4), 677–707. doi: 10.1007/s00382-012-1336-x
Weller, H., McIntyre, W., & Shipley, D. (2020). Multifluids for representing subgrid-scale convection. *Journal of Advances in Modeling Earth Systems*, *12*(8), e2019MS001966. Retrieved from `https://agupubs.onlinelibrary.wiley.com/doi/abs/10.1029/2019MS001966` (e2019MS001966 10.1029/2019MS001966) doi: https://doi.org/10.1029/2019MS001966
Weller, H., & McIntyre, W. A. (2019). Numerical solution of the conditionally averaged equations for representing net mass flux due to convection. *Quarterly Journal of the Royal Meteorological Society*, *145*(721), 1337-1353. doi: 10.1002/qj.3490
Yano, J. (2014). Basic convective element: Bubble or plume? a historical review. *Atmos. Chem. Phys*, *14*(13), 7019–7030. doi: https://doi.org/10.5194/acp-14-7019-2014